Article

Developmental Cell

Treatment during a developmental window prevents NF1-associated optic pathway gliomas by targeting Erk-dependent migrating glial progenitors

Graphical abstract

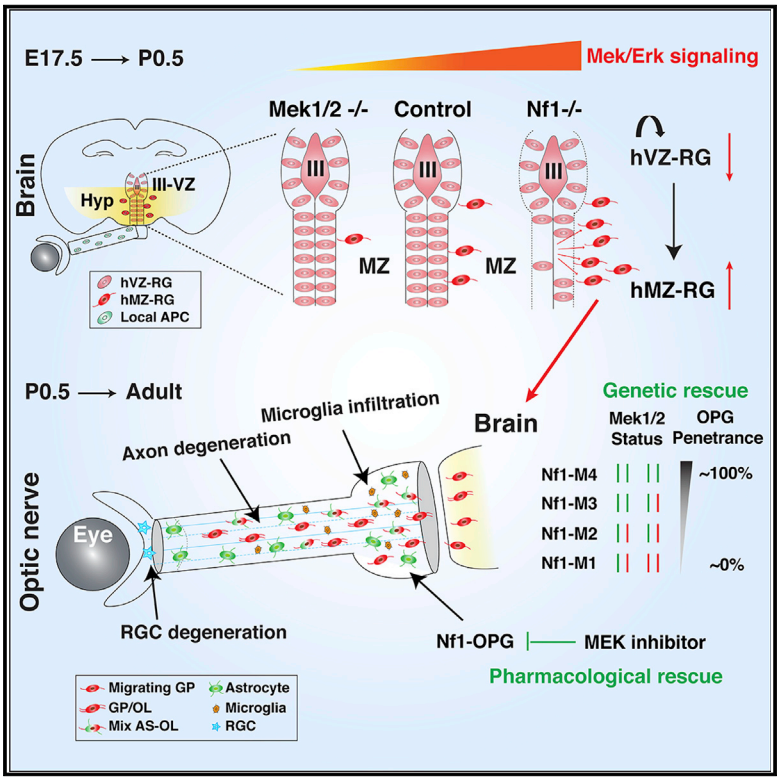

Highlights

- Migrating GPs, not local APCs, are Mek/Erk dependent and thus susceptible to Nf1 loss
- Nf1 is required to maintain the balance between stem-cell maintenance and gliogenesis
- Partial *Mek* loss normalizes differentiation of Nf1$^{-/-}$ migrating GPs and prevents NF1-OPG
- Transient neonatal low-dose MEKi treatment prevents NF1-OPG and neuronal degeneration

Authors

Emmanuelle S. Jecrois, Wang Zheng, Miriam Bornhorst, ..., Hui Zong, Roger J. Packer, Yuan Zhu

Correspondence

yzhu@childrensnational.org

In brief

The mechanism of vulnerability to pediatric low-grade gliomas during development remains unknown. Jecrois et al. demonstrate that NF1-OPG arise from the dependency of Mek-Erk/MAPK signaling during gliogenesis of developmentally transient migrating progenitors in the optic nerve. Transient post-natal treatment with a MEK inhibitor prevents NF1-OPG formation and retinal neuronal degeneration.

Jecrois et al., 2021, Developmental Cell *56*, 1–15
October 25, 2021
https://doi.org/10.1016/j.devcel.2021.08.004

CellPress

Developmental Cell

CellPress

Article

Treatment during a developmental window prevents NF1-associated optic pathway gliomas by targeting Erk-dependent migrating glial progenitors

Emmanuelle S. Jecrois,[1,2,3,4,9] Wang Zheng,[1,2,3,9] Miriam Bornhorst,[1,2,3,5,9] Yinghua Li,[1,2,3] Daniel M. Treisman,[1,2,3] Daphine Muguyo,[1,2,3] Sharon Huynh,[1,2,3] Shayne F. Andrew,[1,2,3] Yuan Wang,[1,2,3] Jingwen Jiang,[1,2,3] Brianna R. Pierce,[1,2,3] Hongmei Mao,[1,2,3] Matthew K. Krause,[1,2,3] Austin Friend,[1,2,3] Francisco Nadal-Nicolas,[6] Steven F. Stasheff,[1,6] Wei Li,[6] Hui Zong,[7] Roger J. Packer,[1] and Yuan Zhu[1,2,3,4,8,10,*]

[1]Gilbert Family Neurofibromatosis Institute, Children's National Hospital, Washington, DC 20010, USA
[2]Center for Cancer and Immunology Research, Children's National Hospital, Washington, DC 20010, USA
[3]Center for Neuroscience Research, Children's National Hospital, Washington, DC 20010, USA
[4]Neuroscience Graduate Program, University of Michigan Medical School, Ann Arbor, MI 48109, USA
[5]Center for Genetic Medicine Research, Children's National Hospital, Washington, DC 20010, USA
[6]Retinal Neurophysiology Section, National Eye Institute, National Institutes of Health, Bethesda, MD 20892, USA
[7]Department of Microbiology, Immunology, and Cancer Biology, University of Virginia, Charlottesville, VA 22908, USA
[8]GW Cancer Center, George Washington University, Washington, DC 20052
[9]These authors contributed equally
[10]Lead contact
*Correspondence: yzhu@childrensnational.org
https://doi.org/10.1016/j.devcel.2021.08.004

SUMMARY

The mechanism of vulnerability to pediatric low-grade gliomas (pLGGs)—the most common brain tumor in children—during development remains largely unknown. Using mouse models of neurofibromatosis type 1 (NF1)-associated pLGGs in the optic pathway (NF1-OPG), we demonstrate that NF1-OPG arose from the vulnerability to the dependency of Mek-Erk/MAPK signaling during gliogenesis of one of the two developmentally transient precursor populations in the optic nerve, brain-derived migrating glial progenitors (GPs), but not local progenitors. Hyperactive Erk/MAPK signaling by *Nf1* loss overproduced GPs by disrupting the balance between stem-cell maintenance and gliogenesis of hypothalamic ventricular zone radial glia (RG). Persistence of RG-like GPs initiated NF1-OPG, causing Bax-dependent apoptosis in retinal ganglion cells. Removal of three *Mek1/Mek2* alleles or transient post-natal treatment with a low-dose MEK inhibitor normalized differentiation of $Nf1^{-/-}$ RG-like GPs, preventing NF1-OPG formation and neuronal degeneration. We provide the proof-of-concept evidence for preventing pLGGs before tumor-associated neurological damage enters an irreversible phase.

INTRODUCTION

In addition to hereditary (H) and environmental (E) factors, replication (R) errors during stem/progenitor cell divisions lead to gradual accumulation of oncogenic driver events over time (Song et al., 2018; Tomasetti et al., 2017). This EHR model provides the mechanistic basis for the observation that the incidence of most cancers dramatically increases with age, as driver mutations occur by chance and accumulate. Pediatric tumors, or tumors that occur almost exclusively in children, are therefore a noteworthy deviation from this pattern (Song et al., 2018; Tomasetti et al., 2017). Brain tumors are the most common solid tumors in children, the most frequent of which are pediatric low-grade gliomas (pLGGs) (Jones et al., 2018; Packer et al., 2020). Most pLGGs are sporadic and driven by gain-of-function mutations in *BRAF*, an oncogene in the RAS-ERK/MAPK signaling pathway, predominantly caused by *KIAA1549-BRAF* fusions or, less frequently, by $BRAF^{V600E}$ point mutations (Ryall et al., 2020). The requirement of only one driver event—termed the one-hit model of tumorigenesis—to develop pLGGs is consistent with the high incidence in children. However, the rarity of pLGGs in adults implies the existence of a vulnerable developmental window during which transient stem/progenitor cell divisions in the central nervous system (CNS) randomly lead to replication errors, but only sufficiently accumulate one driver event in the RAS-ERK/MAPK pathway to form pLGGs in children (Ryall et al., 2020).

Approximately 10%–14% of pLGGs are associated with neurofibromatosis type 1 (NF1), a familial cancer predisposition syndrome caused by germline heterozygous loss-of-function alterations in the *NF1* tumor suppressor gene (Ryall et al., 2020). *NF1* encodes a RAS GTPase-activating protein (RAS-GAP),

Please cite this article in press as: Jecrois et al., Treatment during a developmental window prevents NF1-associated optic pathway gliomas by targeting Erk-dependent migrating glial progenitors, Developmental Cell (2021), https://doi.org/10.1016/j.devcel.2021.08.004

which negatively regulates RAS-mediated signaling pathways by accelerating the conversion of active RAS-GTP to inactive RAS-GDP (Gutmann et al., 2017). NF1-associated tumorigenesis arises from loss of the remaining *NF1* wild-type alleles in somatic cells (also known as a "second hit"), activating the RAS-ERK/MAPK signaling to form *BRAF*-wild-type pLGGs (D'Angelo et al., 2019; Gutmann et al., 2017; Ryall et al., 2020). The majority of NF1-associated pLGGs develop along the optic pathway (NF1-OPG), also known as optic pathway gliomas, which occur in nearly 20% of children with NF1 (Fisher et al., 2012; Sellmer et al., 2018). Of note, NF1-OPGs are predominantly diagnosed in children younger than 7 years of age with few, if any, adult cases (Sellmer et al., 2018). Similar to sporadic pLGGs, the fact that NF1-OPG is almost exclusively restricted to early developmental periods implies two critical cellular and molecular mechanisms: (1) the existence of transient neural stem and progenitor populations in the developing CNS and (2) their susceptibility to hyperactive ERK/MAPK signaling for neoplastic transformation (Figure S1A).

The identity of the ERK-dependent neural stem/progenitor populations vulnerable to pLGG formation in the developing cerebellum and the hypothalamic/chiasmatic/optic nerve regions—the two most frequent sites for pLGGs—remains largely unknown (Ryall et al., 2020; Tchoghandjian et al., 2009). However, the optic nerve (ON) provides a unique system to study the stem/progenitor-of-origin of NF1-OPG because it is comprised cells from two known macroglial lineages but lacks neuronal cell bodies (Figure 1A). The astrocyte population in the ON arises locally from the neuroepithelial cells in the embryonic ON, which give rise to only astrocytes (type 1 astrocytes), via astrocyte precursor cells (APCs), specified by the Pax2 transcription factor (Miller et al., 1989; Tao and Zhang, 2014). By contrast, the oligodendrocyte lineage in the ON is not locally derived, but the descendants of brain-derived migrating progenitors that reach the distal ON at birth (Figure 1A). Since these migrating progenitors can differentiate into type 2 astrocytes and were previously named as oligodendrocyte and type 2 astrocyte (O-2A) progenitors, we refer to these migrating progenitors as glial progenitors (GPs) (Miller et al., 1989). Migrating GPs are known to arise from radial glia (RG) neural stem cells in the ventricular zone of the third ventricle (III-VZ) during late embryonic stages, and then migrates via the optic chiasm into the distal ON (prechiasmatic region) at birth (Marsters et al., 2016; Ono et al., 2018). Using genetically engineered mouse (GEM) models, previous studies have shown abnormal growth properties of neural stem cells in the developing III-VZ upon *Nf1* loss, suggesting that these might be a cell-of-origin for NF1-OPG (Lee et al., 2012). Given that RG stem cells in the developing III-VZ do not migrate into the ON (Marsters et al., 2016; Miller et al., 1989; Ono et al., 2018; Tao and Zhang, 2014), which of the two developmentally transient precursor populations—local progenitors/APCs, brain-derived migrating GPs, or both—form NF1-OPG, remains uncertain.

RESULTS

Pax2$^+$ local progenitors are not affected upon *Nf1* loss

We first investigated the role of local progenitors in NF1-OPG formation by using a Pax2-cre driver to conditionally knockout *Nf1* (*Nf1*^{Pax2}CKO) in Pax2$^+$ APCs (Ohyama and Groves, 2004; Zhu et al., 2001) (Figure S1B). No significant abnormality in Pax2$^+$ cells, Olig2$^+$ cells, or p-Erk levels was observed at post-natal day 0.5 (P0.5), when migrating GPs, marked by Olig2 expression, just arrived the distal ON from the brain of control and *Nf1*^{Pax2}CKO mice (Figures S1C–S1F). To validate that the local Pax2$^+$ lineage was not affected by *Nf1* loss, we used a second Cre transgenic line driven by the human GFAP promoter (hGFAP-cre), which induced OPG with complete penetrance (Zhu et al., 2005). While the onset of hGFAP-cre expression occurred during the neurogenic phase of RG stem cells in the VZ of the dorsal forebrain between embryonic day 12.5 (E12.5) and E13.5, its expression was relatively late in gliogenic RG stem cells in the hypothalamic region between E14.5 and E15.5 (Li et al., 2020; Ma et al., 2021; Marsters et al., 2016; Zhou et al., 2020). As illustrated by β-galactosidase expression and loss of Pten expression in a Rosa26-driven LacZ reporter and a *Pten* CKO model, respectively (Akgül et al., 2018; Li et al., 2020), hGFAP-cre specifically targeted glial lineages in the hypothalamic region of the ventral forebrain, despite exhibiting robust neuronal targeting in the dorsal forebrain (Figure S1G). Thus, the hGFAP-cre-mediated targeting strategy better models human NF1 conditions by avoiding the introduction of homozygous *Nf1* deletion into multiple neuronal populations in the hypothalamic region, which are derived from multipotent RG stem cells in the III-VZ during earlier embryonic stages (Ma et al., 2021; Zhou et al., 2020).

Similarly, hGFAP-cre-mediated expression of a Rosa26-driven td-Tomato reporter (td-Tom$^+$) in the ON was not detected until E15.5 (Figure S1H). By E17.5, the td-Tom$^+$ reporter was extensively expressed in the ON, which was exclusively comprised Pax2$^+$ APCs, but not migrating GPs that expressed brain lipid binding protein (BLBP) and/or Olig2 (Figures 1B, 1C, and S1I). Similar to the P0.5 *Nf1*^{Pax2}CKO ON, we observed no significant alteration in the number, proliferation rate, or Erk activation (p-Erk levels) in *Nf1*-deficient (Nf1$^{-/-}$) Pax2$^+$ APCs in the E17.5 *Nf1*^{hGFAP}CKO ON (Figures 1D, 1E, and S1I–S1K). Of note, BLBP, a marker initially identified for RG stem cells throughout the developing CNS, was highly expressed in RG stem cells in the III-VZ, which were hereafter referred to as hypothalamic ventricular zone radial glia (hVZ-RG) (Figures 1B and 1C). These results show that local progenitor/APCs are not affected by *Nf1* loss and thus are unlikely to be a cell-of-origin for astrocytic tumors in the NF1-OPG model.

BLBP$^+$ migrating GPs are susceptible to *Nf1* loss and depend on Erk signaling

The number of BLBP$^+$ migrating GPs was dramatically increased (>3-fold) in the P0.5 *Nf1*^{hGFAP}CKO ON compared with the control (Figures 1F and 1G). Conversely, BLBP$^+$ migrating GPs were nearly absent in the P0.5 ON of a hGFAP-cre-mediated conditional knockout *Mek1*$^{flox/flox}$/*Mek2*$^{-/-}$ model (M0) lacking Erk signaling (Li et al., 2012) (Figures 1F and 1G). The vast majority (~80%) of migrating GPs expressed BLBP, but less than half of BLBP$^+$ cells also expressed Olig2 (Figures 1H and 1I). Due to low numbers, more differentiated BLBP$^-$Olig2$^+$ cells were not significantly different between the control and *Nf1*^{hGFAP}CKO ON (Figures 1H and 1I). Thus, BLBP$^+$ cells represent the major migrating population(s) from the optic chiasm to the distal ON at birth, undergoing abnormal expansion in the absence of *Nf1*. Conversely, the near-absence of BLBP$^+$ cells in the M0 ON

Please cite this article in press as: Jecrois et al., Treatment during a developmental window prevents NF1-associated optic pathway gliomas by targeting Erk-dependent migrating glial progenitors, Developmental Cell (2021), https://doi.org/10.1016/j.devcel.2021.08.004

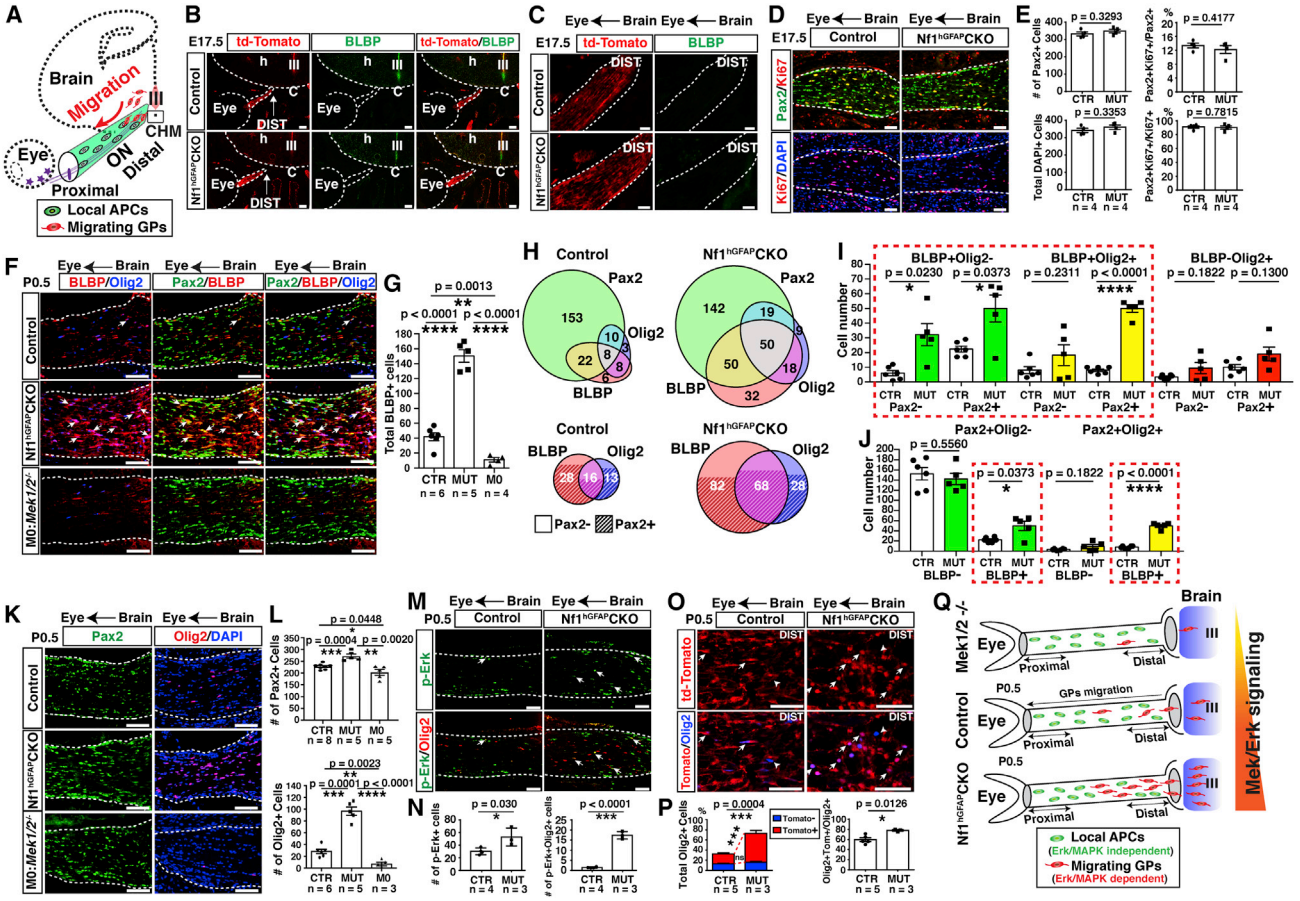

Figure 1. Migrating GPs, not locally derived APCs, are susceptible to *Nf1* loss

(A) Schematic of cellular origins of two macroglial populations in the developing ON. APCs (green) arise locally, while migrating GPs (red) migrate from the ventral brain via the optic chiasm.

(B and C) BLBP and td-Tomato expression in the hypothalamic/chiasm/ON (h/c/ON) region (B) and the distal ON (C).

(D and E) Co-labeling and quantification of Pax2 and Ki67 expression in the distal ON. Dashed lines delineate the ON.

(F–J) Co-labeling of BLBP, Olig2, and Pax2 (F) and quantification of BLBP (G) in the P0.5 distal ON. Arrows mark BLBP$^+$Pax2$^+$Olig2$^+$ cells. Venn diagrams show overlapping expression of Pax2, BLBP, and Olig2 (H). Shaded areas (below) mark Pax2$^+$ cells within BLBP$^+$Olig2$^-$, BLBP$^+$Olig2$^+$, and BLBP$^-$Olig2$^+$ populations. Pax2 expression in BLBP/Olig2 populations (I) and BLBP expression in Pax2/Olig2 populations (J) in the P0.5 distal ON were quantified. Red boxes indicate BLBP$^+$ populations.

(K and L) Co-labeling and quantification of Pax2 or Olig2 in the P0.5 distal ON.

(M and N) Co-labeling and quantification of p-Erk and Olig2 in the P0.5 distal ON. Arrows mark p-Erk$^+$Olig2$^+$ cells.

(O and P) Co-labeling and quantification of td-Tomato and Olig2 in the P0.5 distal ON. Arrows mark td-Tomato$^+$Olig2$^+$ cells. Arrowheads mark td-Tomato$^-$Olig2$^+$ cells.

(Q) Schematic of the impact of different levels of Mek-Erk signaling on migrating GPs.

Quantifications are presented as mean ± SEM. Statistical analysis used unpaired two-tailed Student's t test. Ns, not significant; VB, ventral brain; III, third ventricle; ON, optic nerve; APC, astrocyte precursor cell; GP, glial progenitor; CTR, control group; MUT, *Nf1*^{hGFAP}CKO mutant group; M0, *Mek*1/2 double-knockout group. Scale bar: 50 μm.

See also Figure S1.

suggests that the Mek-Erk/MAPK dependency leads to the vulnerability of the migrating lineage(s) to tumor formation upon *Nf1* loss (Figures 1F and 1G).

Unexpectedly, a major proportion of the increased BLBP$^+$ populations in the *Nf1*^{hGFAP}CKO ON expressed Pax2, which were also present in the control ON (Figures 1H and 1I). Based on the timing (neonatal) and location (distal ON), these observations are most consistent with a model wherein upon arrival to the distal ON, a subset of BLBP$^+$ migrating GPs acquire the local APC marker, Pax2. Three observations supported this model: (1) nearly the entire expansion of the Pax2$^+$ cells was caused by those co-expressing BLBP in the distal ON of P0.5 *Nf1*^{hGFAP}CKO mice (Figure 1J), (2) the similar number of BLBP$^+$ cells was found between P0.5 control and *Nf1*^{Pax2}CKO ON (Figures S1L and S1M), and (3) the increased Pax2$^+$ cells overlapped with the migrating front of Olig2$^+$ cells in the distal ON of P0.5 *Nf1*^{hGFAP}CKO mice (Figures 1K and 1L). In the control distal ON, we calculated that ~15% of the total Pax2$^+$ cells arose from migrating BLBP$^+$/Olig2$^+$ GPs that acquired Pax2 expression (Figure 1H), which was in agreement with an ~11% of

Please cite this article in press as: Jecrois et al., Treatment during a developmental window prevents NF1-associated optic pathway gliomas by targeting Erk-dependent migrating glial progenitors, Developmental Cell (2021), https://doi.org/10.1016/j.devcel.2021.08.004

loss of Pax2$^+$ cells in the P0.5 M0 ON (Figures 1K and 1L). Importantly, abnormal activation of Erk signaling was enriched in Olig2$^+$ cell populations of the P0.5 *Nf1*^{hGFAP}CKO ON (Figures 1M and 1N). This increase was almost exclusively observed in the Nf1$^{-/-}$ compartment, evidenced by the td-Tom$^+$ reporter expression (Figures 1O and 1P). Together, the developmental timing (neonatal) and location (distal ON) of initial expansion observed in the ON of the *Nf1*^{hGFAP}CKO model, not the *Nf1*^{Pax2}CKO model, demonstrate that brain-derived migrating GPs, not local APCs, are susceptible to hyperactive Erk/MAPK signaling for tumor formation as a result of the Mek-Erk/MAPK dependency (Figure 1Q).

Disruption of the balance between stem-cell maintenance and gliogenesis of Nf1$^{-/-}$ hVZ-RG

No increase in the proliferative index of the BLBP$^+$ cells in the P0.5 *Nf1*^{hGFAP}CKO ON suggests a possibility that the expansion of Nf1$^{-/-}$ BLBP$^+$ cells occurs prior to their migration from the brain (Figures S1N and S1O). We therefore investigated how *Nf1* loss impacted BLBP$^+$ cells in the embryonic brain (Figure 2A). Consistent with the onset of hGFAP-cre-mediated recombination at E14.5–E15.5, we observed no abnormality in the hypothalamic region of *Nf1*^{hGFAP}CKO mice at E15.5 (Figures S2A–S2C). However, a dramatic increase in BLBP$^+$ cells was observed in the hypothalamic mantle zone (MZ) of *Nf1*^{hGFAP}CKO brains at E17.5 (Figures 2B and S2D). Importantly, BLBP$^+$ cells in the both control and *Nf1*^{hGFAP}CKO hypothalamic MZ exhibited RG-like morphology, expressing the same RG markers, including Sox9 and hGFAP-Cre, as those by BLBP$^+$ hVZ-RG in the III ventricle (Figures 2B, 2C, and S2D). Indeed, these RG-like cells in the MZ were recently characterized as hypothalamic MZ-RG (hMZ-RG) cells in both the mouse and human embryonic hypothalamic region, which were direct descendants of hVZ-RG cells (Zhou et al., 2020). Thus, the dramatic increase of BLBP$^+$ hMZ-RG-like cells in the E17.5 hypothalamic region is the earliest abnormality detected in the brain of *Nf1*^{hGFAP}CKO mice (Kim et al., 2014; Wang et al., 2012; Zhu et al., 2005).

In the dorsal hypothalamic region, the number and proliferation of hVZ-RG cells (BLBP$^+$Olig2$^-$) in the III ventricle between control and *Nf1*^{hGFAP}CKO mice were not significantly different (Figures 2D–2F). However, the number of BLBP$^+$Olig2$^+$ cells, which were often clustered on the border of the VZ and MZ, was significantly increased in the dorsal hypothalamic region of E17.5 *Nf1*^{hGFAP}CKO brains (Figures 2E and 2F). Importantly, BLBP- and/or Olig2-expressing cells, which were abnormally expanded in the P0.5 distal ON, had already increased in the E17.5 *Nf1*^{hGFAP}CKO hypothalamic MZ (Figures 2E and 2F). BLBP$^+$ cells, regardless of Olig2 expression, exhibited a proliferative rate comparable with control in the both E17.5 hypothalamic MZ and P0.5 distal ON of *Nf1*^{hGFAP}CKO mice (Figures 2E and 2F). Instead, more differentiated BLBP$^-$Olig2$^+$ cells were the only progenitor population showing increased proliferation in the *Nf1*^{hGFAP}CKO hypothalamic MZ at E17.5 (Figure 2F). Given that apoptosis was rare in both control and *Nf1*^{hGFAP}CKO brains, the increased cell numbers, but lack of proliferative advantage, of BLBP$^+$ cells in the hypothalamic MZ, suggests an alternative mechanism. While the normal VZ structure were relatively maintained in the dorsal hypothalamic region (Figures 2E, S2E, and S2F), focal disruption of the VZ structure was consistently found in the ventral hypothalamic region of *Nf1*^{hGFAP}CKO brains at E17.5 (Figures 2B, 2C, and S2D). This abnormal ventricular phenotype was more readily revealed by two markers (Cre and Sox9) that label the nuclei of hVZ-RG and hMZ-RG cells inside and immediately outside the ventral III ventricle, respectively (Figures 2G and 2H). Loss of Cre$^+$Sox9$^+$BLBP$^+$ hVZ-RG stem cells in the focally disrupted III-VZ was accompanied by the increase of Cre$^+$Sox9$^+$BLBP$^+$ hMZ-RG cells in the surrounding MZ (Figures 2G and 2H). These results are most consistent with a model wherein Nf1 loss disrupts the balance of stem-cell maintenance and gliogenesis in the embryonic hypothalamic region, overproducing BLBP$^+$ hMZ-RG cells in the MZ at the expense of hVZ-RG inside the III ventricle. By E17.5, BLBP$^+$ cells in the optic chiasm had not been targeted by hGFAP-cre-mediated recombination but at P0.5 exhibited similar expansion to what was observed in the distal ON of *Nf1*^{hGFAP}CKO mice (Figures S2G–S2J). The 2-day delay in the expansion of BLBP$^+$ cells between the E17.5 hypothalamic MZ and P0.5 optic chiasm/distal ON further support the model that initial expansion of the BLBP$^+$ progenitors must occur in the embryonic brain, but subsequently migrate into the optic chiasm and distal ON at birth.

The MADM-Nf1 model validates altered balance between hVZ-RG and hMZ-RG-like cells

In order to further investigate how *Nf1* loss disrupts the balance between stem-cell maintenance in the VZ and gliogenesis in the MZ of the embryonic hypothalamic region, we developed a model for NF1-OPG by crossing the *Nf1*^{hGFAP}CKO mice with the mosaic analysis with double markers (MADMs) strain (referred to as MADM-Nf1) (Liu et al., 2011). The MADM system provides two unique features. First, due to random and insufficient Cre-mediated recombination between chromosomes during mitotic divisions (Liu et al., 2011), the MADM model generates much fewer (1%–5%) recombined cells than the conventional *Nf1*^{hGFAP}CKO model, which allows for quantification in regions with high cellular density such as the III-VZ. Second, the MADM system generates one Nf1$^{-/-}$ cell and one sibling *Nf1* wild-type (Nf1$^{+/+}$) cell from a common parental *Nf1* heterozygous (Nf1$^{+/-}$) cell at a 1:1 ratio during mitotic divisions, marked by red (R) and green (G) fluorescent protein, respectively (Figure 3A). These features allow for direct comparison of proliferation, differentiation, and morphology between sibling control and mutant cells within the same tissues.

We first used a MADM-wild-type (MADM-WT) model in which both red and green sibling cells were WT for *Nf1* (Liu et al., 2011). In the MADM-WT model, due to the random assortment of symmetric and asymmetric divisions of stem cells, we observed some variations in the R/G ratio between individual brain sections at E17.5 (Figures 3B, 3C, and S3A). However, this individual variation balanced to a net 1:1-R/G ratio (0.988) when we combined multiple sections from each of the 6 MADM-WT brains (Figure 3D). Having validated the MADM-WT system, we next investigated their littermates, the MADM-Nf1 mice. In the hypothalamic region as a whole, Nf1$^{-/-}$ cells only exhibited a minor growth advantage over sibling Nf1$^{+/+}$ cells with a R/G ratio of 1.159. Strikingly, when we compared the R/G ratio inside the III-VZ with that in the surrounding MZ, we consistently observed a reverse patten of the R/G ratio inside the III-VZ with more green Nf1$^{+/+}$ cells versus in the surrounding MZ with more red Nf1$^{-/-}$

Please cite this article in press as: Jecrois et al., Treatment during a developmental window prevents NF1-associated optic pathway gliomas by targeting Erk-dependent migrating glial progenitors, Developmental Cell (2021), https://doi.org/10.1016/j.devcel.2021.08.004

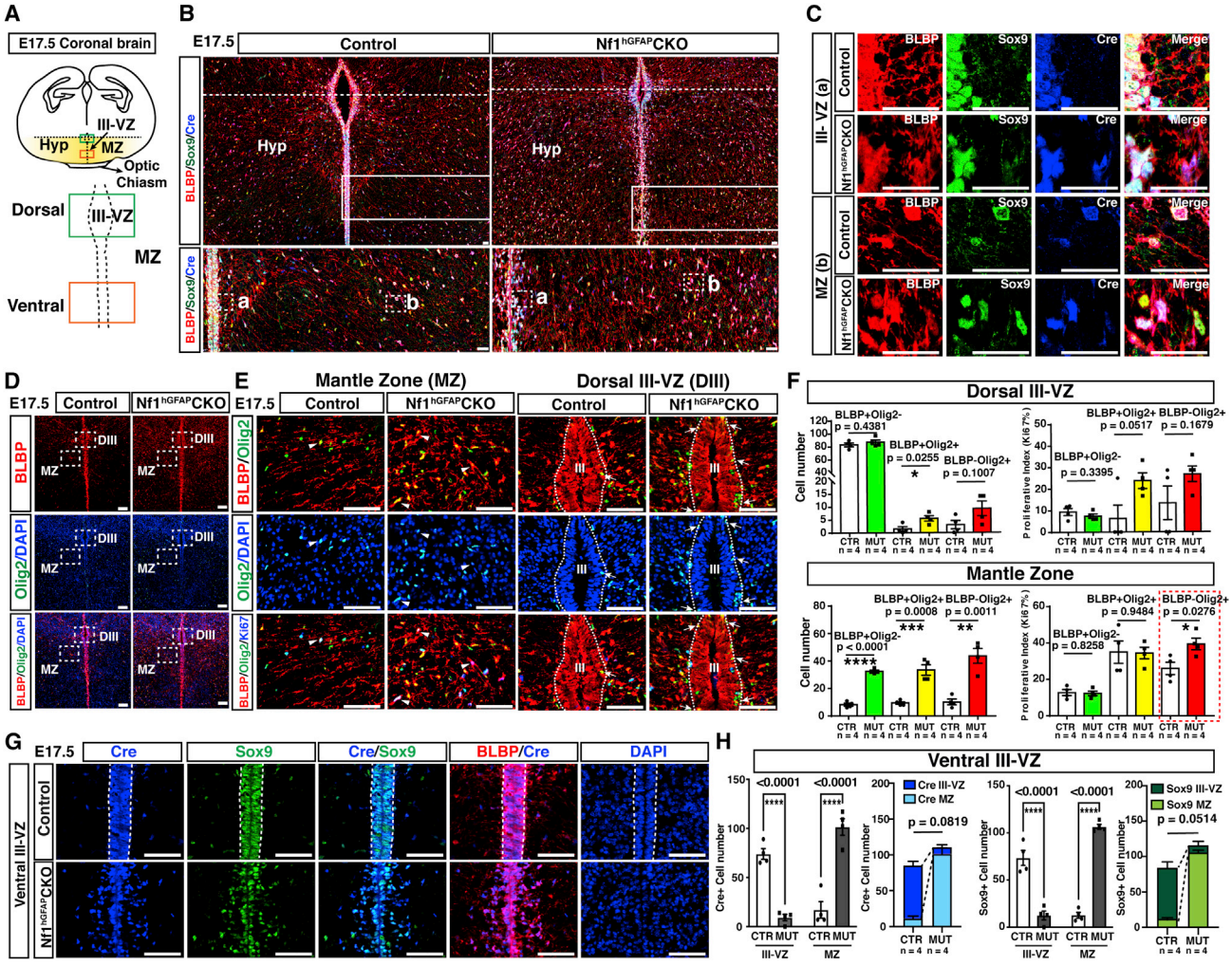

Figure 2. *Nf1* loss disrupts the balance between stem-cell maintenance and gliogenesis of the embryonic hVZ-RG

(A) Schematic of E17.5 mouse coronal brain section with the hypothalamic (h) region highlighting the dorsal III-VZ, ventral III-VZ and the mantle zone (MZ) analyzed.

(B and C) Confocal images of coronal sections from E17.5 control and Nf1^{hGFAP}CKO brains co-labeled with BLBP, Sox9, and Cre. Solid-line boxes indicate enlarged areas (below). Dashed-line boxes (B) are shown (C), showing a RG-like morphology of hVZ-RG in the III-VZ and adjacent MZ (A) and hMZ-RG cells in the MZ (B) of the embryonic hypothalamus.

(D–F) Co-labeling and quantification of BLBP, Olig2, and Ki67 in E17.5 control and Nf1^{hGFAP}CKO hypothalamic regions. Boxes (D) show the dorsal III-VZ and MZ of the hypothalamus (E). Dashed lines (E) denote the border between the III-VZ and surrounding MZ. Arrowheads indicate BLBP^{+}Olig2^{+}Ki67^{+} cells in the MZ. Arrows indicate BLBP^{+}Olig2^{+} cells on the border of the III-VZ.

(G and H) Co-labeling and quantification of BLBP, Sox9, and Cre in the ventral III-VZ and MZ at E17.5.

Quantifications are presented as mean ± SEM. Statistical analysis used unpaired two-tailed Student's t test. III-VZ, third ventricular zone; MZ; mantle zone; hVZ-RG, hypothalamic ventricular zone radial glia; hMZ-RG, hypothalamic mantle zone radial glia; MP, migrating progenitor. Scale bars: 50 μm.

See also Figure S2.

cells, 0.4 versus 1.8, respectively (Figures 3D and 3E). These results provide more direct evidence that *Nf1* loss disrupts the balance between stem-cell maintenance and differentiation, driving hVZ-RG cells out of the III ventricle to become hMZ-RG cells in the MZ (Figure 3F).

While the R/G ratio inside the III-VZ was maintained between 0.4 and 0.45 from E17.5 to P0.5, red Nf1$^{-/-}$ cells continued to expand with a R/G ratio increasing to 3.12 in the MZ of the MADM-Nf1 brain at P0.5 (Figures 3G and 3H). This continuous expansion could at least partially be caused by the higher proliferative rate of Nf1$^{-/-}$ BLBP^{-}Olig2^{+} cells in the MZ (the red box, Figure 2F). Importantly, the sibling green Nf1$^{+/+}$ cells and red Nf1$^{-/-}$ cells were also distinct in the differentiation status. The percentage of the green Nf1$^{+/+}$ cells expressing BLBP was dramatically reduced from 70% inside the III-VZ to 16% in the MZ, while the percentage of green Nf1$^{+/+}$ cells expressing Olig2 was inversely increased from only 9% in the III-VZ to 69% in the MZ (Figures 3I and 3J). This pattern is consistent with normal glial differentiation from hVZ-RG stem cells to more differentiated oligodendrocyte precursor cells (OPCs) (BLBP^{+}Olig2^{-} → BLBP^{+}Olig2^{+} → BLBP^{-}Olig2^{+}). In contrast, the majority of the abnormally expanded red Nf1$^{-/-}$ cells in the MZ expressed both BLBP and

Please cite this article in press as: Jecrois et al., Treatment during a developmental window prevents NF1-associated optic pathway gliomas by targeting Erk-dependent migrating glial progenitors, Developmental Cell (2021), https://doi.org/10.1016/j.devcel.2021.08.004

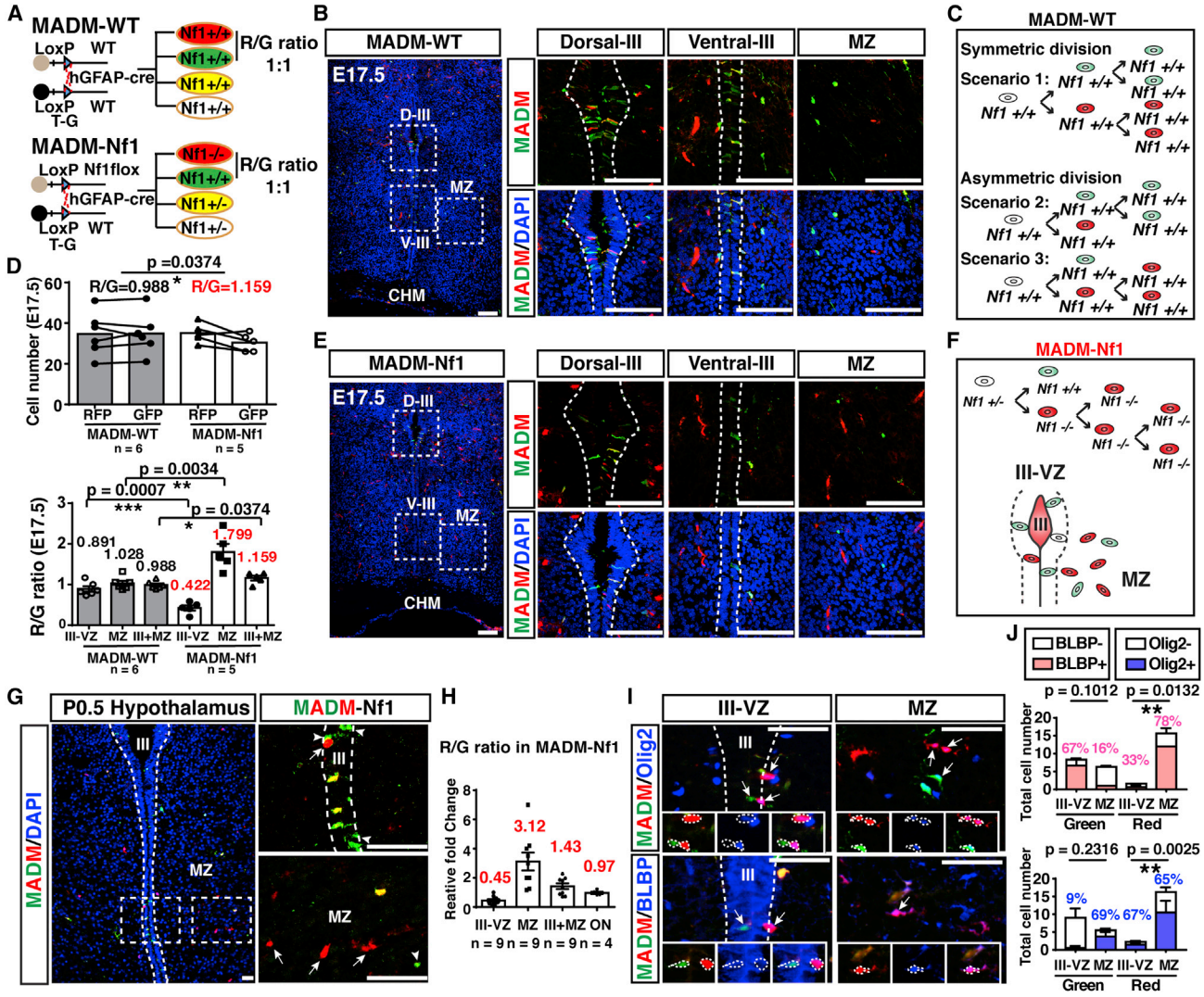

Figure 3. MADM-based model validates the role of *Nf1* in maintaining the balance between hVZ-RG and hMZ-RG cells

(A) Schematic of the MADM-WT and MADM-Nf1 models under the hGFAP-cre driver.

(B–F) Confocal images of coronal sections from MADM-WT (B) and E17.5 MADM-Nf1 (E) hypothalamic regions co-labeled with GFP and RFP. Boxes (left) show the dorsal III-VZ, ventral III-VZ and the MZ (right). Dashed lines delineate the III-VZ. Models summarizes expected outcomes from symmetric and asymmetric division in MADM-WT (C) and MADM-Nf1 (F) models. Total green and red cells and the red/green (R/G) ratio in the III-VZ, the MZ, the ventral brain (III-VZ and MZ combined) and the ON were quantified (D).

(G) Horizontal sections of P0.5 MADM-Nf1 mice were co-labeled with GFP and RFP. Boxes show III-VZ (right, upper) and MZ (right, lower). Arrowheads indicate $Nf1^{+/+}$ cells (green). Arrows label $Nf1^{-/-}$ cells (red).

(H) The R/G ratio was quantified in the III-VZ, the MZ, the ventral brain (III-VZ and MZ combined) and the ON of P0.5 MADM-Nf1 mice.

(I and J) Co-labeling and quantification of GFP/RFP and either Olig2 (top) or BLBP (bottom) on horizontal sections of P0.5 MADM-Nf1 brains (I). Insets show single channel staining of cells (arrows), including a pair of dividing cells on the border of the III-VZ with an $Olig2^{-}$ green cell inside and an $Olig2^{+}$ red cell outside the III-VZ.

Quantifications are presented as mean ± SEM. Statistical analysis used unpaired two-tailed Student's t test. GFP, green fluorescent protein; RFP, red fluorescent protein; hVZ-RG, hypothalamic ventricular zone radial glia; hMZ-RG, hypothalamic mantle zone radial glia; VB, ventral brain; III-VZ, third ventricular zone; D-III, dorsal third ventricular zone; V-III, ventral third ventricular zone; MZ, mantle zone. Scale bars, 50 μm.

See also Figure S3.

Olig2 with each at 78% and 65%, respectively (Figure 3J). When a pair of sibling green and red cells was captured during mitotic division on the border of the III-VZ niche, the red $Nf1^{-/-}$ cell with Olig2 expression was always observed on the border of the niche, while the sibling green $Nf1^{+/+}$ cells lacking Olig2 expression remained inside the niche (Figure 3I). These results suggest premature, but impaired, glial differentiation as a mechanism for the disruption of the balance between stem-cell maintenance and gliogenesis of hVZ-RG cells in the III-VZ. Despite not directly causing increased proliferation, *Nf1* loss increases $BLBP^{+}$ hMZ-RG cells in the hypothalamic region via two mechanisms: (1) overproducing $BLBP^{+}Olig2^{-}$ and $BLBP^{+}Olig2^{+}$ cells in the MZ by

Please cite this article in press as: Jecrois et al., Treatment during a developmental window prevents NF1-associated optic pathway gliomas by targeting Erk-dependent migrating glial progenitors, Developmental Cell (2021), https://doi.org/10.1016/j.devcel.2021.08.004

dislocating hVZ-RG stem cells out of the III ventricle and (2) impairing differentiation of BLBP$^+$ cells in the MZ, which serve as the source of migrating GPs for the ON (Figure S3B).

Nf1$^{-/-}$ cells undergo transient expansion in the neonatal ON and initiate OPG formation

We used the MADM-Nf1 system to further validate the model wherein BLBP$^+$ migrating GPs, but not Pax2$^+$ local APCs, contribute to initial expansion in the *Nf1*-deficient ON. At birth, almost the entire population of red and green cells (>99%) were observed within local Pax2$^+$ populations, but not migrating BLBP$^+$ populations in the distal ON of the MADM-Nf1 model, which was due to infrequent Cre-mediated interchromosomal recombination (Figures S3C and S3D). No difference in the R/G ratio was observed in the P0.5 MADM-Nf1 ON, further validating the model that *Nf1* loss has no effect on local APCs (Figures S3C and S3D). We next used the fluorescence-activated cell sorting (FACS) method to investigate red and green fluorescent cells from the same ON of both MADM-WT and MADM-Nf1 mice at different post-natal stages (P15, P21, and P30) (Figures 4A and 4B). Both green and red Nf1$^{+/+}$ cells in the MADM-WT ON, or green Nf1$^{+/+}$ cells in the MADM-Nf1 ON, were similarly low and comprised 2% to 4% of the total cells (Figures 4A and 4B). While a 1:1-R/G ratio was constantly observed in the MADM-WT ON, a dramatic increase in the R/G ratio was observed in the MADM-Nf1 ON (Figures 4A and 4B). Importantly, the increase of Nf1$^{-/-}$ cells over their sibling Nf1$^{+/+}$ cells reached a plateau with about a 9-fold increase (~20% of the total cells) in the MADM-Nf1 ON during the first three post-natal weeks (Figure 4B). Despite only a small number of cells being targeted with *Nf1* deletion, some MADM-Nf1 mice did develop OPGs with robust GFAP expression similar to those observed in the conventional *Nf1*^{hGFAP}CKO model (Figure S3E). The R/G ratio in the OPGs remains consistent at 7–8 from P30 to P60, indicating this cell population no longer significantly undergoes expansion in the mature ON (Figures 4B and S3F). More importantly, red Nf1$^{-/-}$ cells with expression of BLBP and Olig2 greatly contributed to the tumor masses in the MADM-Nf1 model (Figures S3E and S3F). The MADM-Nf1 system not only validates the model wherein *Nf1* loss in brain-derived migrating progenitors leads to NF1-OPG formation, but also shows that abnormal expansion of migrating GPs mainly occurs during a specific developmental time window in the ON.

Similar to the MADM-Nf1 ON, the *Nf1*^{hGFAP}CKO ON also exhibited abnormal expansion during the first two post-natal weeks and then reached a plateau (Figures 4C, S4A, and S4B). At P0.5 when increased numbers of BLBP$^+$ GPs migrated into the *Nf1*^{hGFAP}CKO ON, relatively normal numbers of microglia expressing Iba1 and P2Y12 (a marker for homeostatic or resting microglia) were observed, but no CD68 (a marker for activated microglia) was detected (Figures 4D–4F). Importantly, CD68 was highly and specifically expressed in the ON with OPG, but not control ON (Figures 4G and 4H). Increased infiltration and accumulation of microglia, evidenced by Iba1 expression, became detectable at P15—after the major expansion of Nf1$^{-/-}$ cells had already occurred (Figures 4I, S4C, and S4D). Abnormal immune response dramatically increased with an activated morphology of Iba1$^+$ microglia at later stages when degeneration of axons, myelin, and RGCs became evident at P60 or later (Figures 4I, 4J, and S4C–S4F). Loss of RGCs in the *Nf1*^{hGFAP}CKO mice was accompanied by apoptosis, which was completely eliminated in the absence of a proapoptotic regulator, Bax (Figures 4K, 4L, and S5A–S5D). As previously published (Péquignot et al., 2003), *Bax* deficiency eliminated naturally occurring apoptosis in RGCs during normal development, leading to increased numbers of RGCs even in the *Nf1*^{hGFAP}CKO model (comparable with that in the *Bax* single-mutant retina) (Figures 4K and 4L). Despite no apoptosis in RGCs, *Bax*/*Nf1*-double mutant mice exhibited a greater ON enlargement with larger tumors accompanied by more severe tumor-associated events, including degeneration of axons and myelin as well as accumulation of activated microglia than those observed in the *Nf1*^{hGFAP}CKO ON (Figures 4K, 4L, and S5A–S5E). Together, these results suggest that developmental defects in Nf1$^{-/-}$ BLBP$^+$-migrating GPs precede an abnormal immune response and axonal degeneration, triggering Bax-mediated apoptosis in RGCs (Figure 4M).

Mouse and human NF1-pLGGs express BLBP with mixed glial precursor characteristics

As a transient developmental precursor population(s), BLBP$^+$ cells were rare in the normal mature ON but were increased by 10-fold and contributed to 25% of *Nf1*^{hGFAP}CKO OPG cells (Figures 5A–5C). The major increase of *Nf1*^{hGFAP}CKO OPG cells expressing GFAP, Olig2 or both was mainly contributed by those co-expressing BLBP (Figures 5D, 5E, and S6A–S6C). The expression pattern of p-Erk in these three glial populations of *Nf1*^{hGFAP}CKO OPGs was remarkably similar to that of BLBP (Figures 5F–5J). Using a BLBP-driven GFP reporter, nearly 40% of p-Erk+ cells co-expressed BLBP-GFP in *Nf1*^{hGFAP}CKO OPGs, which were also rare cells in the control ON (Figures 5K and 5L). Moreover, high levels of BLBP$^+$ and p-Erk$^+$ cells were observed at every stage analyzed during tumor progression (Figures S6D and S6E). These results suggest that abnormal activation of Erk/MAPK signaling not only drives initial expansion of BLBP$^+$ cells during the neonatal stages but also may be responsible for maintaining this transient developmental RG-like population(s) throughout tumorigenesis. Similar to BLBP, Pax2 expression is transient during normal development, becoming a rare marker entirely restricted to GFAP$^+$Olig2$^-$ astrocytes in the control ON (Figures S6F and S6G). Approximately a 3-fold increase of Pax2$^+$ cells was observed in *Nf1*^{hGFAP}CKO OPGs, and, notably, 13% of them expressed both GFAP and Olig2, reminiscent of triple-positive BLBP$^+$Olig2$^+$Pax2$^+$ cells observed in the neonatal *Nf1*-deficient ON (Figures S6F and S6G). Expression of PDGFRα, an OPC marker, was exclusively observed in the Olig2$^+$ oligodendrocyte lineage in the control ON, while in *Nf1*^{hGFAP}CKO OPGs, exhibiting nearly a 4-fold increase with abnormal GFAP expression (Figures 5M and 5N). Together, these results provide further support for the model wherein *Nf1*^{hGFAP}CKO OPGs arise from developmentally transient RG-like GPs with impaired differentiation and exhibit mixed OPC and APC characteristics.

In order to further determine the clinical relevance of our findings, tumor samples were collected from four NF1 patients in three locations: the optic chiasm, the brainstem, and the cerebellum. One NF1-pLGG could not be analyzed due to high blood contamination. The remaining three NF1-pLGG samples were

Please cite this article in press as: Jecrois et al., Treatment during a developmental window prevents NF1-associated optic pathway gliomas by targeting Erk-dependent migrating glial progenitors, Developmental Cell (2021), https://doi.org/10.1016/j.devcel.2021.08.004

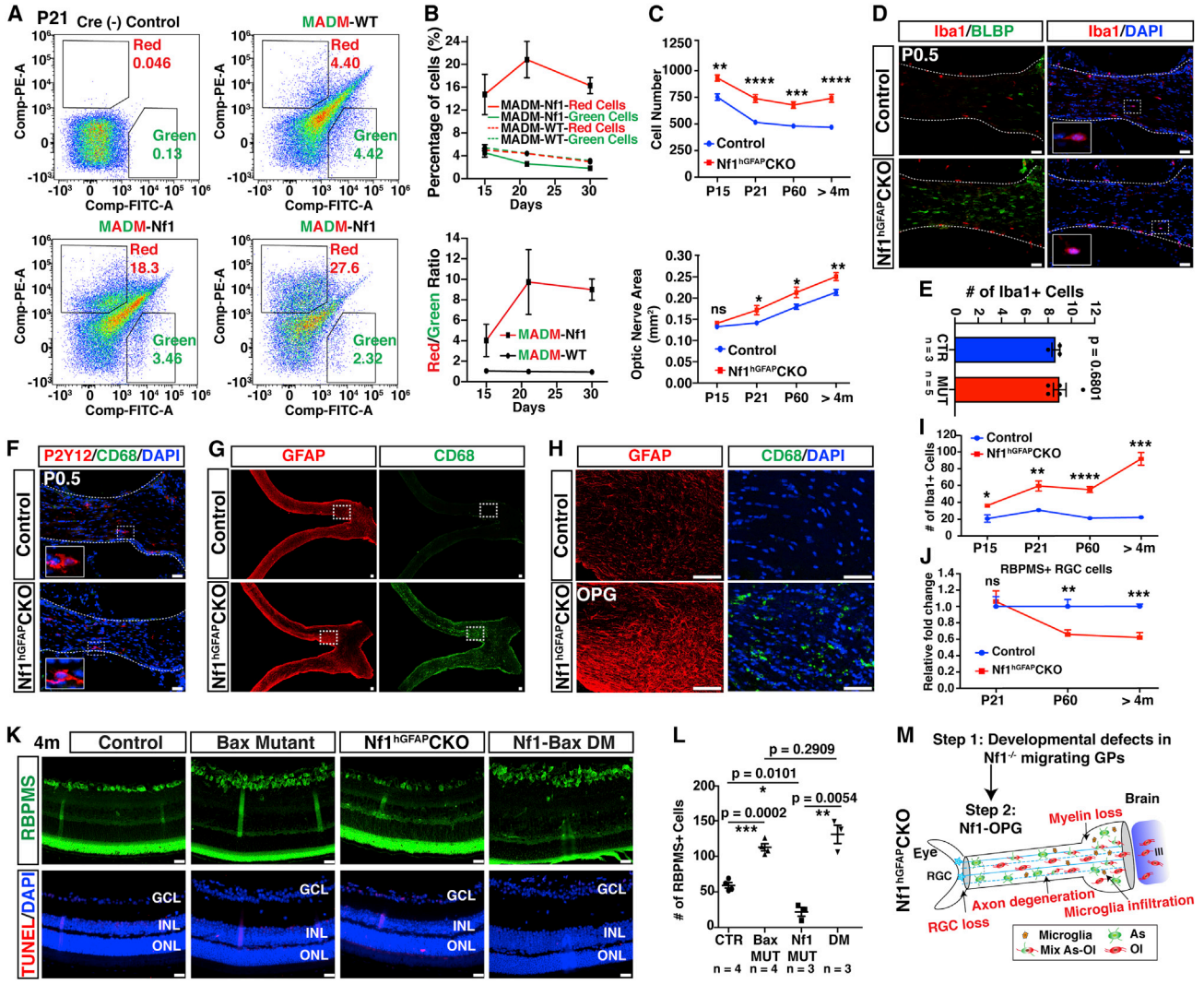

Figure 4. Transient expansion of migrating Nf1$^{-/-}$ cells in the neonatal ON is followed by microglia infiltration, axon/myelin degeneration, and neuronal death

(A and B) FACS analysis of GFP$^+$ and RFP$^+$ cells in the P15, P21, and P30 ON. Representative FACS images show the distribution of red and green cells at P21 in one control, one MADM-WT, and two MADM-Nf1 ONs (A). The percentage of red or green cells and the R/G ratio were quantified (B).

(C) The total cell number and the surface area of the distal ON in control and *Nf1*^{hGFAP}CKO mice at P15, P21, P60, and >4 months were quantified.

(D and E) Co-labeling and quantification of Iba1 and BLBP in P0.5 distal ON (D). Boxed areas are shown in insets.

(F) CD68 and P2Y12 in P0.5 distal ON. Boxed areas are shown in insets.

(G and H) GFAP and CD68 in control and *Nf1*^{hGFAP}CKO ON with an OPG (G). Boxed areas (G) show prechiasmatic regions of the control ON and OPG (H).

(I) The number of Iba1$^+$ microglia were quantified in the ON at different ages.

(J) Relative RBPMS$^+$ RGCs in control and *Nf1*^{hGFAP}CKO retinas at P21, P60, and >4 months were quantified.

(K and L) Co-labeling and quantification of RBPMS and TUNEL in 4-month-old retinas of control, Bax, *Nf1*^{hGFAP}CKO, and *Nf1*^{hGFAP}CKO/Bax mice (K).

(M) A model summarizes the pathogenic sequence of NF1-OPG formation: (1) developmental defects in migrating progenitors and (2) subsequent immune responses of increased microglial infiltration and activation, axonal/myelin degeneration, and RGC loss.

Quantifications are presented as mean ± SEM. Statistical analysis used unpaired two-tailed Student's t test. WT, wild type; RGC, retinal ganglion cell; APC, astrocyte precursor cell; GP, glial progenitor; GP/OL, glial progenitor/oligodendrocyte; AS/OL, astrocyte/oligodendrocyte; GCL, ganglion cell layer; INL, inner nuclear layer; ONL, outer nuclear layer; ns, not significant. Scale bar: 50 μm.

See also Figures S4 and S5.

analyzed and exhibited hyperactive ERK signaling (Figure 5O), as well as robust GFAP and OLIG2 expression (Figure 5P), as previously reported (Ligon et al., 2004; Reitman et al., 2019). Consistent with the literature (Kim et al., 2014; Zhang et al., 2016), GFAP$^+$OLIG2$^+$ astrocytes (Figures S6H and S6I) and BLBP$^+$ cells were rare populations in the normal brain, with the exception of the BLBP$^+$ Bergmann glia in the both human and mouse cerebellum (Figure 5Q). Importantly, two of the three tumors, including one from the optic chiasm, expressed high levels of BLBP with BLBP$^+$OLIG2$^+$ cells (Figure 5R). Thus, similar to the

Please cite this article in press as: Jecrois et al., Treatment during a developmental window prevents NF1-associated optic pathway gliomas by targeting Erk-dependent migrating glial progenitors, Developmental Cell (2021), https://doi.org/10.1016/j.devcel.2021.08.004

CellPress

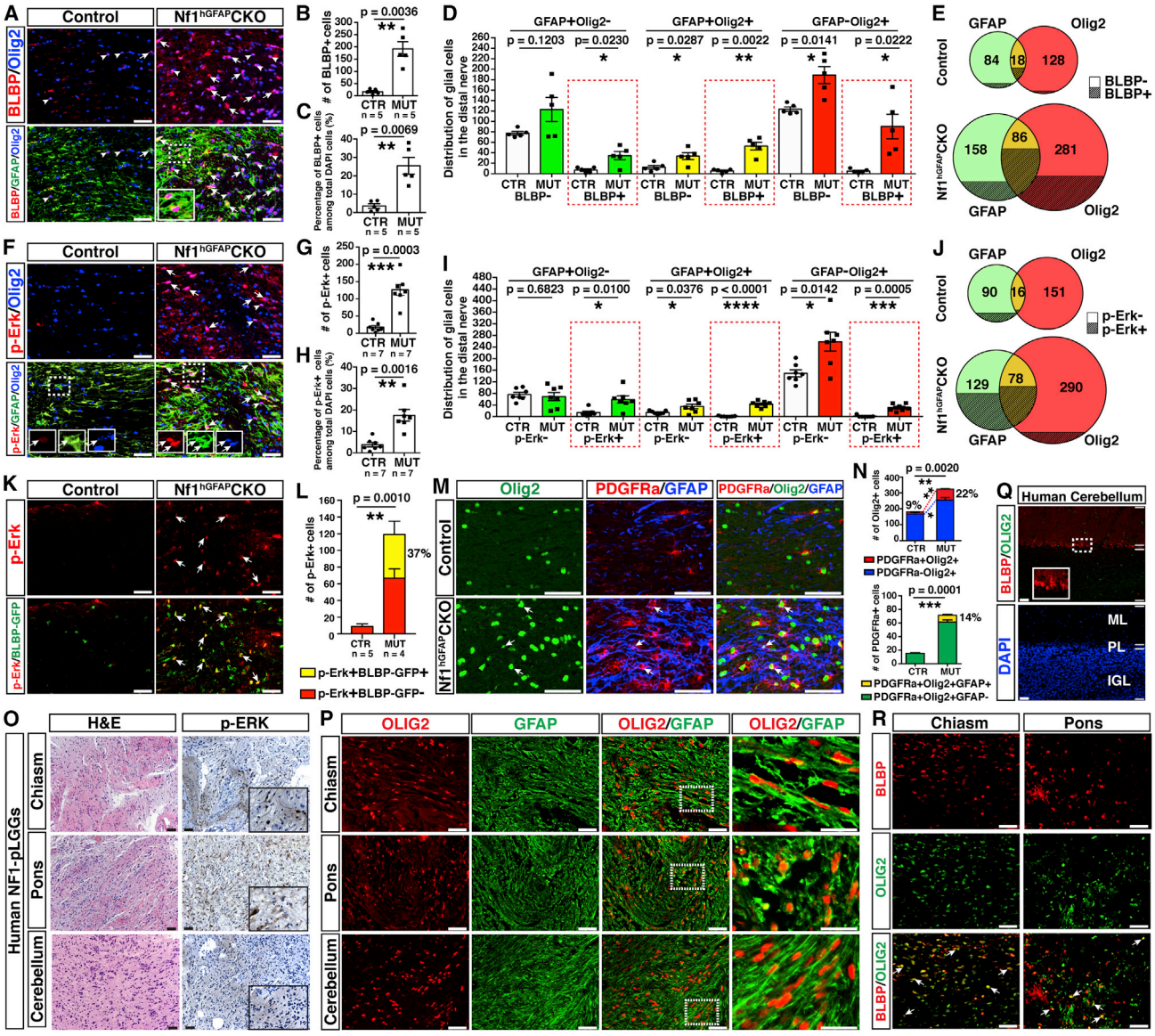

Figure 5. *Nf1*^{hGFAP}CKO OPGs exhibit mixed OPC-APC characteristics with hyperactive Erk

(A–J) Co-labeling and quantification of GFAP, Olig2, and BLBP (A), or GFAP, Olig2, and p-Erk (F) was performed on the ON of control and *Nf1*^{hGFAP}CKO mice (>4 months). Arrowheads and arrows (A) indicate GFAP^{-}Olig2^{+}BLBP^{+} and GFAP^{+}Olig2^{+}BLBP^{+} cells, respectively. Arrowheads and arrows (F) indicate GFAP^{-}Olig2^{+}p-Erk^{+} and GFAP^{+}Olig2^{+}p-Erk^{+} cells, respectively. Boxed areas (A and F) are shown in insets. The number and percentage of BLBP^{+} (B and C) or p-Erk^{+} (G and H) cells were quantified. Quantitative analysis of BLBP^{-} and BLBP^{+} (D and E) or p-Erk^{-} and p-Erk^{+} (I and J) cells in the three GFAP^{+}Olig2^{-}, GFAP^{+}Olig2^{+} and GFAP^{-}Olig2^{+} glial populations was performed on the age-matched control ON and *Nf1*^{hGFAP}CKO OPG. Red boxes show expansion of BLBP-expressing cells (D) or p-Erk-expressing cells (I) from all glial populations of *Nf1*^{hGFAP}CKO OPGs. Venn diagrams summarize expansion of BLBP^{+} (E) or p-Erk^{+} (J) cells (shaded areas) in *Nf1*^{hGFAP}CKO OPGs.

(K and L) Co-labeling and quantification of p-Erk and GFP in the control ON and *Nf1*^{hGFAP}CKO OPG with the BLBP-GFP reporter. Arrows indicate double-positive p-Erk^{+}BLBP-GFP^{+} cells.

(M and N) Co-labeling and quantification of PDGFRα, GFAP and Olig2 in the control ON and *Nf1*^{hGFAP}CKO OPG. Arrows indicate PDGFRα^{+}Olig2^{+}GFAP^{+} cells only found in *Nf1*^{hGFAP}CKO OPGs.

(O) H&E staining and immunohistochemical labeling of p-Erk in human pLGGs from the chiasm, pons, and cerebellum.

(P) GFAP and OLIG2 expression in human pLGGs. Boxed areas are shown (right).

(Q and R) BLBP and OLIG2 in juvenile human cerebellum (Q) and human pLGGs (R). Boxed area (Q) shown in inset. Arrows indicate BLBP^{+}OLIG2^{+} cells (R).

Quantifications are presented as mean ± SEM. Statistical analysis used unpaired two-tailed Student's t test. pLGG, pediatric low-grade glioma; ML, molecular layer; PL, Purkinje cell layer; IGL, internal granule layer. Scale bar, 50 μm.

See also Figure S6.

Please cite this article in press as: Jecrois et al., Treatment during a developmental window prevents NF1-associated optic pathway gliomas by targeting Erk-dependent migrating glial progenitors, Developmental Cell (2021), https://doi.org/10.1016/j.devcel.2021.08.004

Nf1^{hGFAP}CKO mouse model, NF1-associated human pLGGs exhibit the characteristics of migrating RG-like GPs, including BLBP^{+}OLIG2^{+} cells.

Reduction of Erk/MAPK signaling can eliminate tumorigenic potential of Nf1$^{-/-}$ GPs

The sequential events during NF1-OPG formation described above suggest that hyperactivation of Erk/MAPK signaling leads to abnormal expansion, impaired differentiation, and persistence of developmentally transient BLBP^{+} RG-like cells, driving tumor formation. Therefore, we generated *Nf1*^{hGFAP}CKO models with different levels of Erk inhibition to test whether prevention of these developmental defects—the emergence and persistence of BLBP^{+} progenitors—is sufficient to prevent OPG formation. First, we investigated complete elimination of Erk signaling in the M0 model with deletion of all four *Mek1/2* alleles (Li et al., 2012). Regardless of the presence (M0) or absence of *Nf1* (N-M0), the near-complete elimination of BLBP^{+} cells in the hypothalamic MZ validated the essential role of Erk signaling in gliogenesis of hVZ-RG stem cells in the III-VZ (Figures 6A and 6B). However, a lack of Erk signaling also caused early post-natal lethality (median survival of 8 days, Figure 6C), precluding the analysis to prevent OPG formation. To improve survival while maintaining high levels of Erk inhibition, we generated a model with one *Mek* allele, either *Mek1* or *Mek2* (M1), on the *Nf1*^{hGFAP}CKO background (N-M1), as one *Mek* allele was sufficient to rescue the early post-natal lethality of the M0 mouse (Li et al., 2012). We found that N-M1 mice rescued many neurological deficits observed in the *Nf1*^{hGFAP}CKO mice (for comparison referred to as N-M4), including the hindlimb crossing and paralysis associated with infertility in these mice (Kim et al., 2014; Wang et al., 2012). Thus, these results demonstrate that the neurological deficits observed in the *Nf1*^{hGFAP}CKO model are caused by abnormal activation of Erk signaling. All the M1 and N-M1 mice tested survived normally until they developed dermatitis at old age, requiring euthanasia (Figure 6C). More importantly, we found that loss of three *Mek* alleles almost entirely eliminated tumor formation (Figures 6D–6F), and consequently, almost no loss or apoptosis of RGCs was detected in the N-M1 mice (Figures 6G and 6H). Importantly, normalization of the number of BLBP^{+} and/or Olig2^{+} cells in the neonatal ON (Figures 6I and 6J) and the hypothalamic MZ (Figure S7C) provides the mechanistic basis for the prevention of NF1-OPG formation in N-M1 mice.

The *Nf1*^{hGFAP}CKO mice with two or three *Mek* alleles (N-M2 and N-M3) exhibited an intermediate survival rescue. As littermate positive controls, age-matched N-M4 *Nf1*^{hGFAP}CKO mice exhibited robust apoptosis and RGC loss, similar to the *Nf1*^{hGFAP}CKO model before mutant *Mek* alleles were introduced (Figures 6G and 6H). Similar to N-M1 mice, a subset of the N-M2 and N-M3 mice also did not develop tumors or show loss of RGCs (Figures 6D–6H, S7A, and S7B). Of note, the mice that had reduced *Mek* alleles, but did not develop OPGs, all exhibited robust Erk inhibition, while those that still developed tumors all maintained high levels of Erk activation, similar to the N-M4 mice (Figures 6D–6H, and S7A). These results collectively demonstrate that dose-dependent inhibition of Mek-Erk/MAPK signaling rescues the emergence of increased Nf1$^{-/-}$ BLBP^{+} migrating GPs and prevents NF1-OPG formation. Equally importantly, the degree of Erk inhibition required for NF1-OPG formation not only support the viability of the mice but also greatly improve the health and survival of *Nf1*^{hGFAP}CKO mice.

A transient low-dose MEKi treatment of neonatal mice prevents NF1-OPG formation

In order to translate the genetic findings into a potential clinical application, we used a ''MEKi-in-Milk'' protocol, which we previously developed to treat developmental defects of the *Nf1*^{hGFAP}CKO brain (Kim et al., 2014; Wang et al., 2012) (Figures 7A and 7B). Under the ''MEKi-in-milk'' protocol, pups indirectly received MEKi via milk of a lactating mother. Approximately 1%–2% of the mother's MEKi/PD901 dose was delivered to pups, a number estimated based on the observation that a 10-mg/kg PD901 dose given to lactating female mice (Figures S8A and S8B) or direct IP injection at a 0.125 mg/kg dose (Figures S8E and S8F) achieved similar Erk inhibition (50%) in brain tissues. Of note, PD901 was specific for inhibiting Erk/MAPK, but not PI3K/Akt or mTORC1 signaling pathway (marked by p-Akt or p-S6) (Figures S8A–S8D). Similar to the dose-dependent inhibitory effects by the genetic approaches, a dose-dependent effect of MEKi was also observed: 5 mg/kg PD901 (PD5) caused inconsistent Erk/MAPK inhibition, while the 20 mg/kg dose (PD20) exerted the most consistent inhibition of both Erk/MAPK signaling and rescue of tumor phenotypes (Figures S9A–S9D). Unfortunately, most of the PD20-treated mice did not achieve long-term survival into P60.

We therefore selected an intermediate dose of 10 mg/kg PD901 (PD10) to be administered from P0.5–P21. At P21, the PD10 protocol almost completely inhibited Erk activation and rescued the increased cellularity and enlarged ON that were consistently observed in the untreated or vehicle-treated *Nf1*^{hGFAP}CKO mice (Figures S9E–S9G). At P60, nearly 40 days after termination of MEKi treatment, we observed the rescue of enlarged ON size and cellularity (Figures 7C and 7D), as well as sustained inhibition of Erk signaling, the elimination of abnormally expanded GFAP^{+}Olig2^{+} and BLBP^{+} cells in 8 of the 9 MEKi-treated *Nf1*^{hGFAP}CKO mice (Figures 7E–7I). The only exception was correlated with insufficient inhibition of Erk signaling within the ON, which might be due to a lack of MEKi uptake in this treated litter (Figure 7F). The numbers and differentiation of RG-like GPs within the treated ON were normalized (Figures 7E–7I), and as a result, abnormal accumulation of activated microglia, axonal degeneration, and loss of RGCs were all prevented by this protocol with the same one exception (Figures 7J–7M). These results demonstrate that transient neonatal treatment with a low-dose MEKi is sufficient to rescue the developmental defects, which appear to cause NF1-OPG formation and tumor-associated neuronal degeneration.

DISCUSSION

In this study, we employed multiple GEM models, including the MADM-Nf1 model, to identify the brain-derived migrating glial lineage(s) as the lineage-of-origin for NF1-OPG. Based on the Erk dependency and transient developmental window identified for these cells, we designed a transient, low-dose, chemopreventative strategy, which prevented these tumors entirely.

Please cite this article in press as: Jecrois et al., Treatment during a developmental window prevents NF1-associated optic pathway gliomas by targeting Erk-dependent migrating glial progenitors, Developmental Cell (2021), https://doi.org/10.1016/j.devcel.2021.08.004

CellPress

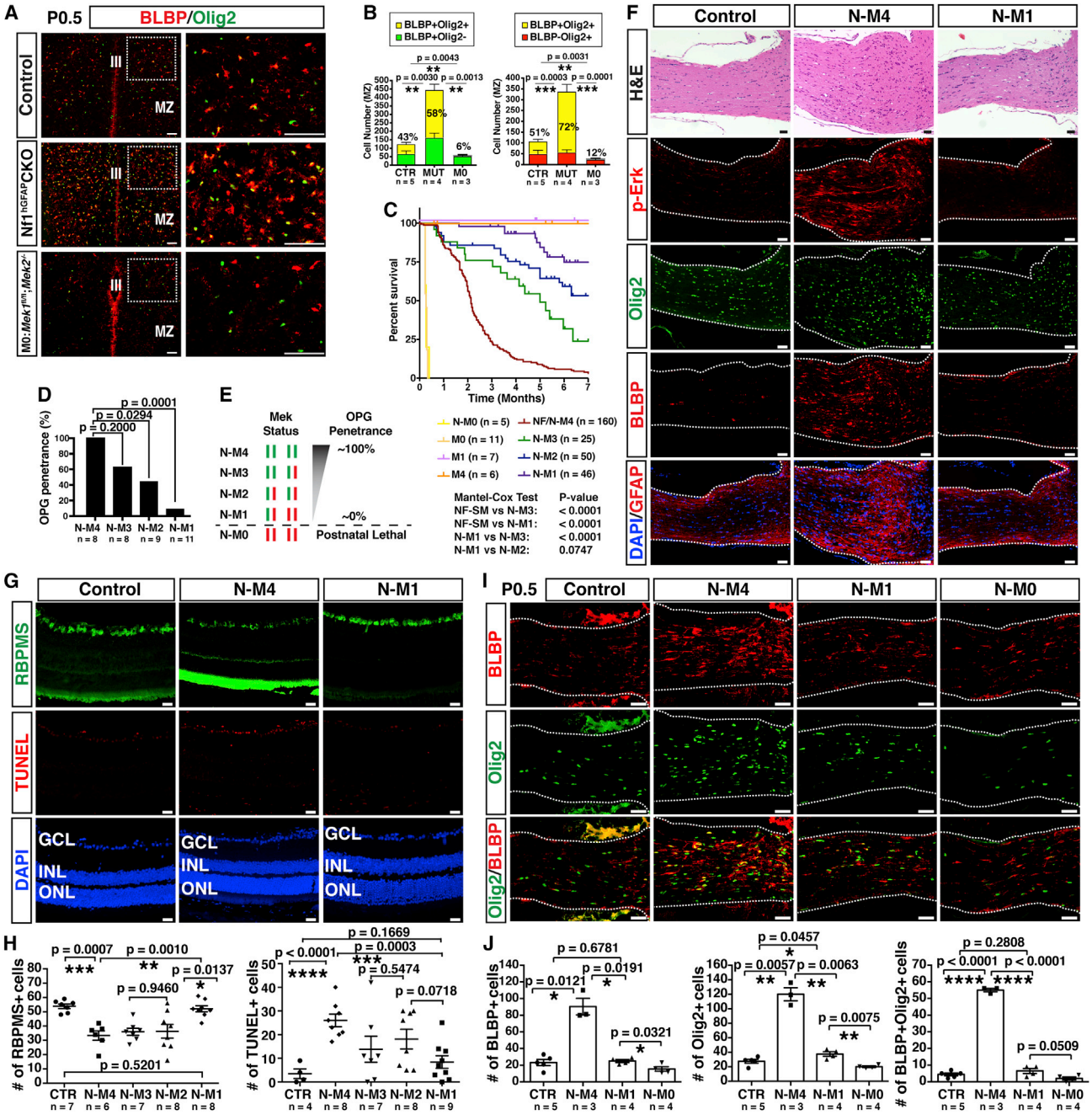

Figure 6. Reduction of Erk/MAPK signaling is sufficient to prevent OPG formation

(A and B) Co-labeling and quantification of BLBP and Olig2 in the hypothalamic regions of P0.5 control, *Nf1*^{hGFAP}CKO, and *Mek*1/2-deficient (M0) mutant mice.

(C) Kaplan-Meir survival curves and Mantel-Cox (log-rank) test for *Mek*1/2 and *Nf1*^{hGFAP}CKO; *Mek*1/2 mutant mice. M0-M4 represents the number of wild-type *Mek*1/2 alleles in each genotype.

(D) Penetrance of OPG in *Nf1*^{hGFAP}CKO mice in N-M4 to N-M1. Statistical analysis used Fisher's exact test.

(E) Schematic of the relationship between *Mek*1/2 alleles in the N-M4 to N-M0 mice and OPG penetrance.

(F) H&E staining and immunolabeling of p-Erk, Olig2, BLBP, and GFAP in the distal ON of age-matched (>4 month) control, N-M4, and N-M1 mice.

(G and H) Co-labeling and quantification of RBPMS and TUNEL from the retinas of control, N-M4, and N-M1 mice.

(I and J) Co-labeling and quantification of BLBP and Olig2 from the distal ON of P0.5 control and N-M4, N-M1, and N-M0 mice.

Quantifications are presented as mean ± SEM. Statistical analysis used unpaired two-tailed Student's t test. III, third ventricle; MZ, mantle zone; GCL, ganglion cell layer; INL, inner nuclear layer; ONL, outer nuclear layer. Scale bar, 50 μm.

See also Figure S7.

Please cite this article in press as: Jecrois et al., Treatment during a developmental window prevents NF1-associated optic pathway gliomas by targeting Erk-dependent migrating glial progenitors, Developmental Cell (2021), https://doi.org/10.1016/j.devcel.2021.08.004

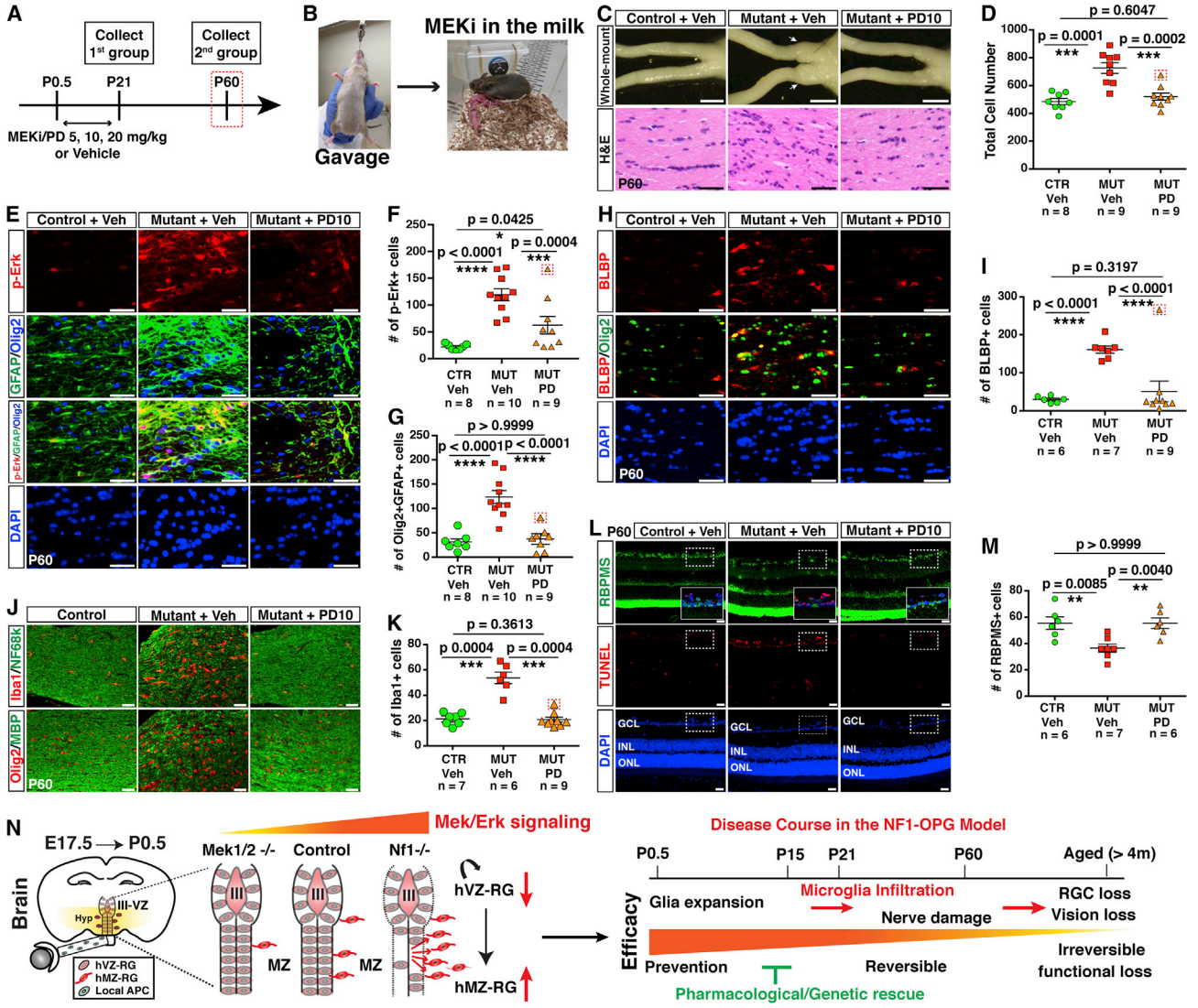

Figure 7. The transient MEKi treatment prevents OPG formation

(A) Experimental design of the P0.5–P21 "MEKi-in-milk" treatment protocol with different doses. Cohorts of vehicle or MEKi-treated mice were collected at either P21 (4 h after last treatment) or P60 (around 40 days after last treatment) for short- and long-term analysis, respectively.

(B) The "MEKi-in-milk" strategy delivers MEKi into newborn pups via lactating females.

(C and D) Whole-mount images and H&E-stained sections of the distal ON from P60 vehicle (VEH) and MEKi (10 mg/kg PD0325901, PD10) treated control and *Nf1*^{hGFAP}CKO mice (C). The total cell number in the distal ON was quantified (D). Red box (D, F, G, I, K, and M) indicates a single non-rescued MEKi-treated *Nf1*^{hGFAP}CKO mouse.

(E–K) Co-labeling and quantification of p-Erk/Olig2/GFAP (E-G), BLBP/Olig2 (H and I), Iba1/NF68k (J, above, and K), and Olig2/MBP (J, below) in the distal ON of P60 vehicle- and MEKi-treated control and *Nf1*^{hGFAP}CKO mice.

(L and M) Co-labeling and quantification of RBPMS and TUNEL in the retinas of P60 vehicle- and MEKi-treated control and *Nf1*^{hGFAP}CKO mice. Boxed areas are shown in insets.

(N) A model for the pathogenic sequence of NF1-OPG formation and the potential efficacy of therapeutic strategies delivered at different disease stages.

Quantifications are presented as mean ± SEM. Statistical analysis used unpaired two-tailed Student's t test. MEKi, MEK inhibitor; GCL, ganglion cell layer; INL, inner nuclear layer; ONL, outer nuclear layer; hVZ-RG, hypothalamic ventricular zone radial glia; GP, glial progenitor; APC, astrocyte precursor cell; OPC, oligodendrocyte precursor cell; III-VZ, third ventricular zone; MZ, mantle zone. Scale bar, 50 μm.

See also Figures S8 and S9.

Erk-dependent migrating GPs causes vulnerability to pLGG formation during development

We used two molecular mechanisms to determine which of the two transient precursor cell populations in the developing ON was vulnerable to NF1-OPG formation: (1) susceptibility to *Nf1* loss and (2) Erk signaling dependency. First, we show that loss of *Nf1* in local Pax2^{+} APCs caused no abnormality in the ON of the *Nf1*^{Pax2}CKO model, whereas the expanded cell population in the ON of the *Nf1*^{hGFAP}CKO model was not observed until P0.5, the time when migrating GPs arrive from the brain

during normal development. Second, in a completely *Mek*-deficient model (the M0 model), the local APCs were largely unaffected, whereas the migrating BLBP^{+} progenitors were almost entirely absent, affirming that the migrating GPs are the transient progenitor cell-lineage-of-origin vulnerable to NF1-OPG formation as a result of Mek/Erk dependency. Given that NF1 is a negative regulator of RAS-mediated Erk/MAPK signaling, Erk signaling dependency is of particular interest in identifying the cell lineage of origin for NF1-OPG. A recent comprehensive analysis of the molecular mechanisms and clinical correlates of 1,000 pLGGs demonstrated that upregulation of the RAS-ERK/MAPK pathway is nearly universal in these childhood tumors (Ryall et al., 2020), suggesting that Erk signaling dependency can be used as a tool to identify the lineage(s)-of-origin for sporadic pLGGs arising from different regions of the developing brain.

Consistent with the model wherein NF1-OPG arise from migrating GPs, we observed the earliest defect from *Nf1* loss in the hypothalamic region during embryonic stages. Using the conventional the *Nf1*^{hGFAP}CKO model and the MADM-Nf1 model, we observed that the earliest phenotype caused by *Nf1* loss is a disruption in the balance between stem-cell maintenance and gliogenesis in the III-VZ. Upon *Nf1* loss, the hVZ-RG cells generate an initial expanded pool of BLBP^{+} progenitors by disproportionally dislocating out of the III ventricle to become hMZ-RG cells in the hypothalamic MZ at the expense of depleting III-VZ population. These BLBP^{+} progenitors, despite exhibiting no significant increase in proliferation, maintain RG-like characteristics, migrate from the MZ into the optic chiasm and finally enter the ON at P0.5, where they initiate OPG formation. Importantly, our model demonstrates that it is the persistence of BLBP^{+} RG-like progenitors that drives NF1-OPG formation, a finding consistent with a recent study showing that pLGGs from the hypothalamic and chiasmic region exhibited a RG-like signature, while those from the other common pLGG site, the cerebellum, did not (Tchoghandjian et al., 2009).

Clinical implication

NF1-OPG or pLGG in general, despite their non-malignant (benign) status, pose a great clinical challenge, as they cause substantial morbidity in many children (Fisher et al., 2012; Jones et al., 2018; Packer et al., 2020). To date, an ideal therapy to prevent or alleviate tumor/therapy-induced neurological deficits, preserving the quality of life for these affected children, has yet to be discovered. Here, we show that the persistence of Nf1$^{-/-}$ BLBP^{+} RG-like cells appeared to drive OPG initiation, preceding the downstream tumor-associated events: (1) increased infiltration and activation of microglia accompanied by myelin and axonal degeneration and (2) Bax-mediated apoptosis in RGCs (Figure 7N). This finding opens up the exciting possibility for a more effective therapeutic strategy, one that prevents NF1-OPG formation by targeting the earliest developmental defect in the immature ON long before tumor-associated neurological damages enter an irreversible phase. The essential role of Erk/MAPK signaling in the lineage genesis of BLBP^{+} hVZ-RG stem cells in the III ventricle provided a challenge in balancing tumor prevention with viability. In this study, however, we identified a rough threshold level of Mek-Erk/MAPK signaling at which abnormal differentiation and expansion of Nf1$^{-/-}$ BLBP^{+} progenitors were almost completely normalized and OPGs were prevented, while maintaining the viability and rescuing fertiblity of the *Nf1*^{hGFAP}CKO mice, by removing three *Mek* alleles. Of note, the rescue effect was also observed when only one or two *Mek* alleles were removed, albeit with greater variability among mice, thereby demonstrating a dose-dependent effect. By using a very low dose of MEKi during the neonatal stages via the "MEKi-in-Milk" protocol, we show that this treatment protocol, despite its temporary nature, achieved long-term prevention of NF1-OPG formation and tumor-associated RGC loss. Thus, we provide the proof-of-principle necessary to inform chemoprevention therapeutic trials for children with NF1-OPG. The ongoing clinical trials using MEKi at 10–20 times higher doses than the one used in this study on infants with NF1 (as young as 1 month of age) will provide the necessary safety information for the feasibility of this chemopreventative strategy (Fangusaro et al., 2021). The low-dose and transient nature of the "MEKi-in-Milk" protocol also avoids long-lasting MEKi treatment and its potential adverse effects on the developing CNS. This principle may be applicable to children with the developmental disorders with high risks of developing pediatric tumors, such as other RASopathies (i.e., Costello syndrome) that exhibits much more severe neurodevelopmental defects (Castel et al., 2020; Gripp et al., 2019; Gross et al., 2020; Kim et al., 2014; Wang et al., 2012).

Limitations of the study

It will be important to validate these mouse studies in the developing human brain.

STAR★METHODS

Detailed methods are provided in the online version of this paper and include the following:

- KEY RESOURCES TABLE
- RESOURCE AVAILABILITY
  - Lead contact
  - Material availability
  - Data and Code Availability
- EXPERIMENTAL MODELS AND SUBJECT DETAILS
  - Nf1^{hGFAP}CKO
  - Nf1^{Pax2}CKO
  - Nf1^{hGFAP}CKO-*Mek1/2*
  - MADM-*Nf1*
  - Human pLGG Samples
- METHOD DETAILS
  - Genotyping and PCR
  - MEK inhibitor treatment
  - Tissue preparation and processing from adult, embryonic and neonatal tissues
  - Whole-mount imaging, histopathological analysis, and immunofluorescence
  - Mosaic analysis with double markers (MADM) staining
  - TUNEL assay
  - Western blotting
  - Flow cytometry
- QUANTIFICATION AND STATISTICAL ANALYSIS

SUPPLEMENTAL INFORMATION

Supplemental information can be found online at https://doi.org/10.1016/j.devcel.2021.08.004.

ACKNOWLEDGMENTS

We thank J. Lau and Dr. Y. Huang for technical assistance, Dr. A. Groves for providing the Pax2-cre mice, Dr. W.D. Snider for the *Mek1*$^{flox/flox}$/*Mek2*$^{-/-}$ mice, Dr. B. Novitch for the Olig2 antibody, and members of the Zhu lab for support. This work is supported by grants from the DOD NFRP (W81XWH1810685), the NIH Neuroscience training grant (T32-NS076401), Francis S. Collins Neurofibromatosis Therapeutic Association Program, Hyundai Hope On Wheels Young Investigator Award, and the National Science Foundation Graduate Research Fellowship Program.

AUTHOR CONTRIBUTIONS

E.S.J., W.Z., M.B., and Y.Z. conceived and designed the study. E.S.J., W.Z., M.B., and Y.L. performed the experiments. E.J., W.Z., M.B., Y.L., D.M.T., and Y.Z. analyzed the results. S.F.A., Y.W., J.J., D.M.T, S.F.S., W.L., H.Z., and R.J.P. assisted with supervision and resources. D.M., A.F., M.K., F.N., and S.H. provided technical assistance. Y.Z. acquired the funding and wrote the manuscript with contributions from all of the authors.

DECLARATION OF INTERESTS

The authors declare no competing interests.

Received: February 19, 2021
Revised: July 11, 2021
Accepted: August 3, 2021
Published: August 23, 2021

REFERENCES

Akgül, S., Li, Y., Zheng, S., Kool, M., Treisman, D.M., Li, C., Wang, Y., Gröbner, S., Ikenoue, T., Shen, Y., et al. (2018). Opposing tumor-promoting and -Suppressive functions of Rictor/mTORC2 signaling in adult glioma and pediatric SHH medulloblastoma. Cell Rep *24*, 463–478.e5.

Castel, P., Rauen, K.A., and McCormick, F. (2020). The duality of human oncoproteins: drivers of cancer and congenital disorders. Nat. Rev. Cancer *20*, 383–397.

D'Angelo, F., Ceccarelli, M., Tala, Garofano, L., Zhang, J., Frattini, V., Caruso, F.P., Lewis, G., Alfaro, K.D., Bauchet, L., et al. (2019). The molecular landscape of glioma in patients with Neurofibromatosis 1. Nat Med *25*, 176–187.

Fangusaro, J., Onar-Thomas, A., Poussaint, T.Y., Wu, S., Ligon, A.H., Lindeman, N., Campagne, O., Banerjee, A., Gururangan, S., Kilburn, L., et al. (2021). A phase 2 trial of selumetinib in children with recurrent optic pathway and hypothalamic low-grade glioma without NF1: a pediatric brain tumor consortium study. Neuro-Oncology. https://doi.org/10.1093/neuonc/noab047.

Fisher, M.J., Loguidice, M., Gutmann, D.H., Listernick, R., Ferner, R.E., Ullrich, N.J., Packer, R.J., Tabori, U., Hoffman, R.O., Ardern-Holmes, S.L., et al. (2012). Visual outcomes in children with neurofibromatosis type 1-associated optic pathway glioma following chemotherapy: a multicenter retrospective analysis. Neuro-Oncology *14*, 790–797.

Gripp, K.W., Morse, L.A., Axelrad, M., Chatfield, K.C., Chidekel, A., Dobyns, W., Doyle, D., Kerr, B., Lin, A.E., Schwartz, D.D., et al. (2019). Costello syndrome: clinical phenotype, genotype, and management guidelines. Am. J. Med. Genet. A *179*, 1725–1744.

Gross, A.M., Frone, M., Gripp, K.W., Gelb, B.D., Schoyer, L., Schill, L., Stronach, B., Biesecker, L.G., Esposito, D., Hernandez, E.R., et al. (2020). Advancing RAS/RASopathy therapies: an NCI-sponsored intramural and extramural collaboration for the study of RASopathies. Am. J. Med. Genet. A *182*, 866–876.

Gutmann, D.H., Ferner, R.E., Listernick, R.H., Korf, B.R., Wolters, P.L., and Johnson, K.J. (2017). Neurofibromatosis type 1. Nat. Rev. Dis. Primers *3*, 17004.

Jones, D.T.W., Kieran, M.W., Bouffet, E., Alexandrescu, S., Bandopadhayay, P., Bornhorst, M., Ellison, D., Fangusaro, J., Fisher, M.J., Foreman, N., et al. (2018). Pediatric low-grade gliomas: next biologically driven steps. Neuro-Oncology *20*, 160–173.

Kim, E., Wang, Y., Kim, S.J., Bornhorst, M., Jecrois, E.S., Anthony, T.E., Wang, C., Li, Y.E., Guan, J.L., Murphy, G.G., and Zhu, Y. (2014). Transient inhibition of the ERK pathway prevents cerebellar developmental defects and improves long-term motor functions in murine models of neurofibromatosis type 1. eLife *3*, e05151.

Lee, D.Y., Gianino, S.M., and Gutmann, D.H. (2012). Innate neural stem cell heterogeneity determines the patterning of glioma formation in children. Cancer Cell *22*, 131–138.

Li, X., Newbern, J.M., Wu, Y., Morgan-Smith, M., Zhong, J., Charron, J., and Snider, W.D. (2012). MEK is a key regulator of gliogenesis in the developing brain. Neuron *75*, 1035–1050.

Li, Y., Li, B., Li, W., Wang, Y., Akgül, S., Treisman, D.M., Heist, K.A., Pierce, B.R., Hoff, B., Ho, C.-Y., et al. (2020). Murine models of IDH-wild-type glioblastoma exhibit spatial segregation of tumor initiation and manifestation during evolution. Nat. Commun. *11*, 3669.

Ligon, K.L., Alberta, J.A., Kho, A.T., Weiss, J., Kwaan, M.R., Nutt, C.L., Louis, D.N., Stiles, C.D., and Rowitch, D.H. (2004). The oligodendroglial lineage marker OLIG2 is universally expressed in diffuse gliomas. J. Neuropathol. Exp. Neurol. *63*, 499–509.

Liu, C., Sage, J.C., Miller, M.R., Verhaak, R.G., Hippenmeyer, S., Vogel, H., Foreman, O., Bronson, R.T., Nishiyama, A., Luo, L., and Zhong, H. (2011). Mosaic analysis with double markers reveals tumor cell of origin in glioma. Cell *146*, 209–221.

Ma, T., Wong, S.Z.H., Lee, B., Ming, G.L., and Song, H. (2021). Decoding neuronal composition and ontogeny of individual hypothalamic nuclei. Neuron *109*, 1150–1167.e6.

Marsters, C.M., Rosin, J.M., Thornton, H.F., Aslanpour, S., Klenin, N., Wilkinson, G., Schuurmans, C., Pittman, Q.J., and Kurrasch, D.M. (2016). Oligodendrocyte development in the embryonic tuberal hypothalamus and the influence of Ascl1. Neural Dev *11*, 20.

Micallef, L., and Rodgers, P. (2014). eulerAPE: drawing area-proportional 3-Venn diagrams using ellipses. PLoS One *9*, e101717.

Miller, R.H., Ffrench-Constant, C., and Raff, M.C. (1989). The macroglial cells of the rat optic nerve. Annu. Rev. Neurosci. *12*, 517–534.

Ohyama, T., and Groves, A.K. (2004). Generation of Pax2-Cre mice by modification of a Pax2 bacterial artificial chromosome. Genesis *38*, 195–199.

Ono, K., Hirahara, Y., Gotoh, H., Nomura, T., Takebayashi, H., Yamada, H., and Ikenaka, K. (2018). Origin of oligodendrocytes in the vertebrate optic nerve: a review. Neurochem. Res. *43*, 3–11.

Packer, R.J., Iavarone, A., Jones, D.T.W., Blakeley, J.O., Bouffet, E., Fisher, M.J., Hwang, E., Hawkins, C., Kilburn, L., MacDonald, T., et al. (2020). Implications of new understandings of gliomas in children and adults with NF1: report of a consensus conference. Neuro-Oncology *22*, 773–784.

Péquignot, M.O., Provost, A.C., Sallé, S., Taupin, P., Sainton, K.M., Marchant, D., Martinou, J.C., Ameisen, J.C., Jais, J.P., and Abitbol, M. (2003). Major role of BAX in apoptosis during retinal development and in establishment of a functional postnatal retina. Dev. Dyn. *228*, 231–238.

Reitman, Z.J., Paolella, B.R., Bergthold, G., Pelton, K., Becker, S., Jones, R., Sinai, C.E., Malkin, H., Huang, Y., Grimmet, L., et al. (2019). Mitogenic and progenitor gene programmes in single pilocytic astrocytoma cells. Nat. Commun. *10*, 3731.

Ryall, S., Zapotocky, M., Fukuoka, K., Nobre, L., Guerreiro Stucklin, A., Bennett, J., Siddaway, R., Li, C., Pajovic, S., Arnoldo, A., et al. (2020). Integrated molecular and clinical analysis of 1,000 pediatric low-grade gliomas. Cancer Cell *37*, 569–583.e5.

Sellmer, L., Farschtschi, S., Marangoni, M., Heran, M.K.S., Birch, P., Wenzel, R., Mautner, V.F., and Friedman, J.M. (2018). Serial MRIs provide novel insight

into natural history of optic pathway gliomas in patients with neurofibromatosis 1. Orphanet J. Rare Dis. *13*, 62.

Song, M., Vogelstein, B., Giovannucci, E.L., Willett, W.C., and Tomasetti, C. (2018). Cancer prevention: molecular and epidemiologic consensus. Science *361*, 1317–1318.

Tao, C., and Zhang, X. (2014). Development of astrocytes in the vertebrate eye. Dev. Dyn. *243*, 1501–1510.

Tchoghandjian, A., Fernandez, C., Colin, C., El Ayachi, I., Voutsinos-Porche, B., Fina, F., Scavarda, D., Piercecchi-Marti, M.D., Intagliata, D., Ouafik, L., et al. (2009). Pilocytic astrocytoma of the optic pathway: a tumour deriving from radial glia cells with a specific gene signature. Brain *132*, 1523–1535.

Tomasetti, C., Li, L., and Vogelstein, B. (2017). Stem cell divisions, somatic mutations, cancer etiology, and cancer prevention. Science *355*, 1330–1334.

Wang, Y., Kim, E., Wang, X., Novitch, B.G., Yoshikawa, K., Chang, L.S., and Zhu, Y. (2012). ERK inhibition rescues defects in fate specification of Nf1-deficient neural progenitors and brain abnormalities. Cell *150*, 816–830.

Wang, Y., Yang, J., Zheng, H., Tomasek, G.J., Zhang, P., McKeever, P.E., Lee, E.Y., and Zhu, Y. (2009). Expression of mutant p53 proteins implicates a lineage relationship between neural stem cells and malignant astrocytic glioma in a murine model. Cancer Cell *15*, 514–526.

Zhang, Y., Sloan, S.A., Clarke, L.E., Caneda, C., Plaza, C.A., Blumenthal, P.D., Vogel, H., Steinberg, G.K., Edwards, M.S., Li, G., et al. (2016). Purification and characterization of progenitor and mature human astrocytes reveals transcriptional and functional differences with mouse. Neuron *89*, 37–53.

Zhou, X., Zhong, S., Peng, H., Liu, J., Ding, W., Sun, L., Ma, Q., Liu, Z., Chen, R., Wu, Q., and Wang, X. (2020). Cellular and molecular properties of neural progenitors in the developing mammalian hypothalamus. Nat. Commun. *11*, 4063.

Zhu, Y., Harada, T., Liu, L., Lush, M.E., Guignard, F., Harada, C., Burns, D.K., Bajenaru, M.L., Gutmann, D.H., and Parada, L.F. (2005). Inactivation of NF1 in CNS causes increased glial progenitor proliferation and optic glioma formation. Development *132*, 5577–5588.

Zhu, Y., Romero, M.I., Ghosh, P., Ye, Z., Charnay, P., Rushing, E.J., Marth, J.D., and Parada, L.F. (2001). Ablation of NF1 function in neurons induces abnormal development of cerebral cortex and reactive gliosis in the brain. Genes Dev *15*, 859–876.

Please cite this article in press as: Jecrois et al., Treatment during a developmental window prevents NF1-associated optic pathway gliomas by targeting Erk-dependent migrating glial progenitors, Developmental Cell (2021), https://doi.org/10.1016/j.devcel.2021.08.004

STAR★METHODS

KEY RESOURCES TABLE

Reagent or resource	Source	Identifier
Antibodies		
Rabbit anti-PTEN	Cell Signaling	9559; RRID: AB_390810
Mouse anti-Olig2	Millipore	MABN50; RRID: AB_10807410
Goat anti-Olig2	R&D systems	AF2418; RRID: AB_2157554
Rabbit anti-Olig2	Millipore	AB9610; RRID: AB_570666
Guinea pig anti-Olig2	Dr. B. Novitch	Homemade
Goat anti- PDGFRα	R&D systems	AF1062; RRID: AB_2236897
Mouse anti-GFAP	BD PharMingen	556330; RRID: AB_396368
Mouse anti-Ki67	BD PharMingen	550609; RRID: AB_393778
Rabbit anti-Ki67	Abcam	16667; RRID: AB_302459
Rabbit anti-Iba1	Wako	013-27691
Goat anti-Pax2	R&D systems	AF3364; RRID: AB_10889828
Rabbit anti-Pax2	BioLegend	PRB-276P; RRID: AB_291611
Guinea pig anti-RBPMS	Cedarlane	1832
Chicken anti-GFP	Abcam	AB13970; RRID: AB_300798
Rabbit anti-GFP	Millipore	MAB3580; RRID: AB_94936
Mouse anti-RFP	Abcam	AB125244; RRID: AB_10973556
Rabbit anti-RFP	Abcam	AB62341; RRID: AB_945213
Rat anti-MBP	Millipore	MAB386; RRID: AB_94975
Chicken anti-Neurofilament 68kDa (NF68k)	Abcam	AB72997; RRID: AB_1267598
Rat anti-CD68	Bio-Rad	MCA1957; RRID: AB_322219
Rabbit anti-Cre	BioLegend	908001; RRID: AB_2565079
Rabbit anti-P2Y12	AnaSpec	AS-55043A
Goat anti-Sox9	R&D systems	AF3075; RRID: AB_2194160
Rabbit anti-pErk1/2$^{T202/Ty204}$	Cell Signaling	9101S; RRID: AB_331646
Rabbit anti-Erk1/2	Cell Signaling	9102L; RRID: AB_330744
Mouse anti-BLBP	LifeSpan Biosciences	LS-B6684-50; RRID: AB_11143615
Rabbit anti-BLBP	Millipore	ABN14; RRID: AB_10000325
Rabbit anti-pAkt^{S473}	Cell Signaling	4060L; RRID: AB_2315049
Rabbit anti-Akt	Cell Signaling	9272S; RRID: AB_329827
Rabbit anti-S6	Cell Signaling	2217S; RRID: AB_331355
Rabbit anti-pS6$^{S240/244}$	Cell Signaling	5364S; RRID: AB_10694233
Mouse anti-β-Actin	Sigma-Aldrich	A5316; RRID: AB_476743
Alexa Fluor 488	Invitrogen, Life Technologies	A11001; RRID: AB_2535850; A11034; RRID: AB_2576217
Alexa Fluor 555	Invitrogen, Life Technologies	A21429; RRID: AB_2535850; A21424; RRID: AB_141780
Alexa Fluor 647	Invitrogen, Life Technologies	A31571; RRID: AB_162542; A21236; RRID: AB_2535805; A21247; RRID: AB_141778; A21245; RRID: AB_2535813
HRP-conjugated secondary antibodies	BioRad	1706515; RRID: AB_2617112; 1706516; RRID: AB_11125547
Fc receptor blocking	BioLegend	101320; RRID: AB_1574975
Rat PE-anti-CD3	BioLegend	100206; RRID: AB_1574975
Hamster FITC-anti-CD3	Invitrogen	11-0031-85; RRID: AB_464883

(*Continued on next page*)

Continued

Reagent or resource	Source	Identifier
Chemicals, Peptides, and Recombinant Proteins		
PD0325901	Sigma	PZ0162
Critical commercial assays		
Click-it® TUNEL Alexa Fluor®	Invitrogen, Life Technologies	C10247
Experimental models: Organisms/strains		
Mouse; Nf1	Zhu et al., 2001	N/A
Mouse; hGFAP-cre	Wang et al., 2009	N/A
Mouse; Pax2-cre	Ohyama and Groves, 2004	N/A
Mouse; Mek1/Mek2	Li et al., 2012	N/A
Mouse; MADM	Liu et al., 2011	
Oligonucleotides		
Primers for genotyping PCR see method details	This paper	N/A
Software and algorithms		
ImageJ (Version 1.52c)	N/A	https://imagej.nih.gov/ij/
Graphpad Prism 8.0	GraphPad Software Inc.	https://www.graphpad.com/scientific-software/prism/
EulerAPE	N/A	http://www.eulerdiagrams.org/eulerAPE/

RESOURCE AVAILABILITY

Lead contact

Further information and requests for resources and reagents should be directed to the Lead Contact, Yuan Zhu, Ph.D. (yzhu@childrensnational.org).

Material availability

All the reagents and mice generated in this study are available upon request.

Data and Code Availability

The original data generated in this study are available upon request.

EXPERIMENTAL MODELS AND SUBJECT DETAILS

$Nf1^{hGFAP}$CKO

The $Nf1^{hGFAP}$CKO mice were previously described (Kim et al., 2014; Wang et al., 2012; Zhu et al., 2005). The control mice used in this study are a pool of phenotypically indistinguishable mice with genotypes $Nf1^{flox/flox}$; $Nf1^{flox/+}$; and hGFAP-cre^{+}; $Nf1^{flox/+}$. The $Nf1^{hGFAP}$CKO mice used was of the genotype hGFAP-cre^{+}; $Nf1^{flox/flox}$ and was maintained in the mixed backgrounds of C57Bl6, 129Svj, and FVB.

$Nf1^{Pax2}$CKO

$Nf1^{Pax2}$CKO mice were generated by crossing Pax2-cre (Ohyama and Groves, 2004) and $Nf1^{flox/flox}$ mice. The control mice used in this study are a pool of phenotypically indistinguishable mice with genotypes $Nf1^{flox/flox}$; $Nf1^{flox/+}$; and Pax2-cre^{+}; $Nf1^{flox/+}$. The mutant $Nf1^{Pax2}$CKO used was of the genotype Pax2-cre^{+}; $Nf1^{flox/flox}$ and was maintained in the mixed backgrounds of C57Bl6, 129Svj, CD1 and FVB.

$Nf1^{hGFAP}$CKO-*Mek1/2*

The $Mek1^{flox/flox}$ and Mek2$^{-/-}$ mice were described previously (Li et al., 2012). They were later crossed into the hGFAP-cre or $Nf1^{hGFAP}$CKO background described above to generate four groups of mutant mice with different numbers of *Mek1/2* alleles:

M0 (hGFAP-cre^{+};$Mek1^{flox/flox}$;Mek2$^{-/-}$)
N-M0 (hGFAP-cre^{+};$Nf1^{flox/flox}$;$Mek1^{flox/flox}$;Mek2$^{-/-}$)
N-M1 (hGFAP-cre^{+};$Nf1^{flox/flox}$;$Mek1^{flox/flox}$;Mek2$^{-/+}$ or hGFAP-cre^{+};$Nf1^{flox/flox}$;$Mek1^{flox/+}$;Mek2$^{-/-}$)
N-M2 (hGFAP-cre^{+};$Nf1^{flox/flox}$;$Mek1^{flox/+}$;Mek2$^{-/+}$, or hGFAP-cre^{+};$Nf1^{flox/flox}$;$Mek1^{flox/flox}$;Mek2$^{+/+}$, or hGFAP-cre^{+};$Nf1^{flox/flox}$;Mek1$^{+/+}$;Mek2$^{-/-}$)
N-M3 (hGFAP-cre^{+};$Nf1^{flox/flox}$;$Mek1^{flox/+}$;Mek2$^{+/+}$, or hGFAP-cre^{+};$Nf1^{flox/flox}$;Mek1$^{+/+}$;Mek2$^{-/+}$)
N-M4 (hGFAP-cre^{+};$Nf1^{flox/flox}$;Mek1$^{+/+}$;Mek2$^{+/+}$)

Please cite this article in press as: Jecrois et al., Treatment during a developmental window prevents NF1-associated optic pathway gliomas by targeting Erk-dependent migrating glial progenitors, Developmental Cell (2021), https://doi.org/10.1016/j.devcel.2021.08.004

MADM-*Nf1*

The MADM mice used in this study were previously described (Liu et al., 2011). TG mice were crossed with hGFAP-cre^{+};*Nf1*$^{flox/+}$ mice. They were subsequently crossed with GT mice to generate TG/GT hGFAP-cre^{+};*Nf1*$^{flox/+}$ mice for MADM analysis. Cre negative mice and Cre positive Nf1$^{+/+}$ MADM mice were used for controls.

All mice in this study were cared for according to the guidelines that were approved by the Animal Care and Use Committees of the University of Michigan at Ann Arbor as well as the Institutional Animal Care and Use Committee of Children's National Medical Center in Washington, DC. Age and littermate-matched control and mutant mice were used for the developmental analyses to minimize the impact of modifier genes. Similar numbers of mice with both genders were used for the experiments.

Human pLGG Samples

FFPE (Formalin-fixed paraffin-embedded) tissue specimens from NF1 patients diagnosed with low-grade gliomas (LGGs) were obtained from the Department of Pathology at the Children's National Hospital at Washington DC. The case list included a pLGG from the pons of a 5-year-old female, a pLGG from the cerebellum of 10-year-old, and two pLGGs from the chiasms of a 14-year-old female and an 18-year-old male. The de-identified specimens were collected under the exempt Children's National Hospital Institutional Review Board Protocol "Cellular Analysis of Low-Grade Gliomas," Pro 00008541; PI: Miriam Bornhorst, MD. Normal tissue samples for comparison (pons, cerebellum, optic nerve) were collected from pediatric patients who consented for post-mortem tissue collection through Pro 00001339; PI: Javad Nazarian, PhD. Hematoxylin and Eosin staining was performed in each tissue location to ensure that the tissues were not infiltrated with tumor.

METHOD DETAILS

Genotyping and PCR

Genetic analysis of mice in the colony used genomic DNA extracted from tail snips incubated overnight at 50°C in SDS-EDTA TAE Buffer with Proteinase K (Roche Diagnostics). The resulting solution was mixed with isopropanol (1:1) to allow DNA to precipitate. The precipitate was then transferred and diluted into ultrapure water before PCR analysis was performed for each individual target listed below using the Taq 2X MeanGreen Master Mix (Empyrical BioScience) or 2X PCR Super Master Mix (Bimake) in conjuncture with the following primers:

Cre primers	
Icres	5′-CCG TTT GCC GGT CGT GGG-3′
IcreAs	5′-CG TAT ATC CTG GCA GCG ATC- 3′
Pax2-Cre primers	
IRES forward	5′-CCGAAGCCGCTTGGAATAA-3′
IRES reverse	5′-CCCAGATCAGATCCCATACAATG-3′
Nf1 Primers	
Yuan 11	5′-CTT CAG ACT GAT TGT TGT ACC TGA- 3′
Yuan 6.1	5′-AAA TCA GCA GAG GTT GTC AGA ATC- 3′
Yuan 6.2	5′-AGT TCC ATC ACA CGT AAA ATT GAG- 3′
tdTomato Primers	
RT 1	5′-AAG GGA GCT GCA GFG GAG TA- 3′
RT 2	5′-CCG AAA ATC TGT GGG AAG TC- 3′
RT 3	5′-GGC ATT AAA GCA GCG TAT CC- 3′
RT 4	5′-CTG TTC CTG TAC GGC ATG G- 3′
GFP Primers	
eGFP-F	5′-GAG CTG GAC GGC GAC GTA AAC- 3′
eGFP-R	5′-CGT TGT GGC TGT TGT TAG TGT TAC- 3′
Mek1/2 Primers	
Mek1-Olig9	5′-CAG AAG TTC CCA CGA CAC TA- 3′
Mek1-2772Flox	5′-GTC TGT CAC TTG TCT TCT GG- 3′
Mek2WT-13131	5′-CTG ACC TTC CTG TAG GTG- 3′
Mek2WT-13424	5′-ACT CAC GGA CAT GTA GGA- 3′
Mek2KO-Neo25	5′-CGT GCA ATC CAT CTT GTT C- 3′

(*Continued on next page*)

Continued	
MADM primers	
Chr11_CS1	5′-TGGAGGAGGACAAACTGGTCAC-3′
Rosa4	5′-TCAATGGGCGGGG GTCGTT-3′
Chr11_CS2	5′-TTCCCTTTCTGCTTCATCTTGC-3′

MEK inhibitor treatment

MEK inhibitor (MEKi) PD0325901 (Sigma, PZ0162-25MG) was dissolved in 0.5% hydroxypropyl methyl-cellulose plus 0.2% Tween 80 (Sigma) at a concentration of 1mg/ml. The solution was administered by oral gavage at the dosage of 5, 10 or 20 mg/kg (body weight) every day from P0.5-P21 to lactating females (termed the "MEKi-in-milk" protocol) (Kim et al., 2014; Wang et al., 2012). Mice that received vehicle (0.5% hydroxypropyl methyl-cellulose plus 0.2% Tween 80) treatment were used as controls. Entire litter received either vehicle or MEKi treatment. For the MEKi pharmacodynamic studies, PD0325901 (10mg/kg) or vehicle was given to the lactating females via gavage or directly administered to the pups via intraperitoneal injection (IP) using various doses at 0.125mg/kg, 0.25mg/kg, 0.5mg/kg and 1mg/kg as indicated in the figure.

Tissue preparation and processing from adult, embryonic and neonatal tissues

Adult mice (>P15) were perfused with 4% paraformaldehyde (PFA), then optic nerves and brains were dissected, followed by overnight post-fixation in 4% PFA at 4°C. Optic nerves, retinas, and brains were processed through a sequence of dehydration steps prior to paraffin embedding. Optic nerves were separated into two portions and embedded separately: the distal nerves, including the prechiasmatic nerve and the chiasm, and the proximal portion, which included the retina and the optic nerve head (ONH). Paraffin embedded optic nerves were sectioned horizontally and brains were sectioned sagittally or coronally at 5 μm thickness by using a rotary microtome (Leica RM2235). For cross-sectional analysis, eyes from pigmented mice were embedded whole in paraffin and sectioned horizontal to the ONH. Tissues were sectioned at 5 μm thickness. Two criteria were used to select slides for histological analysis: (1) presence of the ONH, and (2) a single layer of RGC in the GCL. For cryostat sections, tissues were fixed overnight in 4% PFA at 4°C, cryoprotected in 30% sucrose and embedded in Tissue-Tek OCT compound (Sakura). Tissues were sectioned at 10 μm thickness using a cryostat (Leica CM 1950). All sections were collected on Superfrost Plus microscope slides (Fisher Scientific).

To prepare for cryostat sections from embryonic and neonatal optic nerves, entire heads, excluding the lower mandible, were embedded. Tissue embedding molds (Polysciences) were coated with OCT and the head was positioned ventral side-down on top of the OCT. The remaining OCT was carefully poured over the head to avoid bubbles until none of the tissue remained exposed. The molds were placed in a dry ice-methanol bath for rapid freezing, then transferred to -80°C for storage. To analyze embryonic or neonatal brains, the brain was carefully dissected out of the skull, placed ventral side up in a brain slicer matrix (Zivic), and the forebrain was divided into two portions. Each brain portion was individually cryopreserved for sectioning. Cryopreserved samples were sectioned at 8 μm thickness.

For protein analysis, P8 pups treated with single dose of MEKi or vehicle through gavage or IP injection were sacrificed between 2–6 h after treatment. Mice were perfused with PBS and the cerebellum and spleen were frozen immediately in liquid nitrogen. Samples were stored in -80°C freezer for western blotting analysis.

Whole-mount imaging, histopathological analysis, and immunofluorescence

Chiasms and optic nerves were micro-dissected, cleaned, and imaged using an Olympus BX-51 fluorescence microscope for whole-mount imaging. The paraffin sections of brain and optic nerve were subjected to histopathological analysis with hematoxylin and eosin (H&E) staining. For immunofluorescence, paraffin sections were deparaffinized through Xylene, 100% ethanol, 95% ethanol, 50% ethanol and 30% ethanol and rehydrated in distilled water. Antigen retrieval was performed with Retrieve-all antigen retrieval solution (BioLegend) in heated coplin jars. Cryosections do not require deparaffinization or antigen retrieval steps and were therefore directly fixed in 4% PFA for 15 min. Sections were then permeabilized by 0.3% Triton-X (Sigma) solution for 20 min and blocked for 1 h with 3% normal goat/horse/donkey serum (Sigma) depending on the secondary antibody selection. Slides were put in a humidified chamber and incubated in primary antibodies, dissolved in the blocking solution, at 4°C overnight. The visualization of primary antibodies for colorimetric labeling was performed with biotinylated secondary antibody (Vector, 1:400), treated with an avidin-biotin complex (Vector), and then subjected to DAB staining (VWR). Hematoxylin was used as a counterstain. The visualization of primary antibodies for immunofluorescence was performed by using Alexa 488, Alexa 555 and Alexa 647-conjugated secondary antibodies (Invitrogen, Life-Technologies) at 1:400 dilution and incubated for 1-hour at room temperature. Slides were washed three times in between the steps with 1X PBS. DAPI (1:2000) was used as a counterstain to label individual cell nuclei. Sections were examined under a light and fluorescent microscope (Olympus BX-63).

The embryonic (E17.5) hypothalamic regions (Figures 2 and 3) were imaged with a 20X objective using a LSM 780 Zeiss confocal microscope equipped with computer-driven motorized stage controlled by Zen Lite software (Black edition, Zeiss). Magnifications images (Figure 2) were taken from ventral part of the third ventricular zone and mantle zone areas using a 40X objective for Sox9/BLBP/Cre markers co-expression analysis.

The primary antibodies used in this study were:
BLBP (ABN14, 1:400, rabbit, EMD Millipore),
BLBP (LS-B6684-50, 1:400, mouse, LifeSpan Biosciences),
CD68 (MCA1957, 1:600, rat, Bio-Rad),
Cre (908001, 1:400, rabbit, BioLegend),
GFAP (556330, 1:2000, mouse, BD Pharmingen),
GFP (MAB3580, 1:500, rabbit, EMD Millipore),
GFP (AB13970, 1:500, chicken, Abcam),
Iba1 (013-27691, 1:2000, rabbit, Wako),
Ki67 (550609, 1:500, mouse, BD Pharmingen),
Ki67 (75019, 1:500, rabbit, Abcam),
MBP (MAB386, 1:500, rat, EMD Millipore),
Neurofilament 68kDa (NF68k) (ab72997, 1: 500, Abcam),
Olig2 (AB9610, 1:2000, rabbit, EMD Millipore),
Olig2 (MABN50, 1:300, mouse, EMD Millipore),
Olig2 (1:10000, guinea pig, a kind home-made gift from Dr. B. Novitch),
Olig2 (AF2418, 1:400, goat, R&D systems),
Pax2 (PRB-276P, 1:400, rabbit, BioLegend),
Pax2 (AF3364, 1:400, goat, R&D systems),
PDGFRα (AF1062, 1:1000, goat, RD),
PTEN (9559, 1:400, rabbit, Cell Signaling), p-Erk (9101S, 1:200, rabbit, Cell Signaling),
P2Y12 (AS-55043A, 1:1000, rabbit, AnaSpec), RBPMS (1832, 1:250, guinea pig, Cedarlane),
RFP (AB62341, 1:400, rabbit, Abcam),
RFP (AB125244, 1:400, mouse, Abcam),
Sox9 (AF3075, 1:400, goat, R&D systems).

Mosaic analysis with double markers (MADM) staining

Cryosections were used for immunofluorescence analysis involving the MADM model (for GFP and RFP). GFP and RFP signals were detected by anti-GFP and anti-RFP primary antibodies, which occupied the commonly used green (488 nm laser) and red (555 nm laser) channels under a fluorescent microscope. Staining with additional markers was visualized in the Far-red channel (635 nm laser) using the appropriate secondary antibody.

TUNEL assay

Terminal deoxynucleotidyl transferase (TdT) dUTP Nick-End Labeling (TUNEL) assay was performed on paraffin sections of retinas using the Click-iT® TUNEL Alexa Fluor® Imaging kit from Invitrogen (C10247), according to manufacturer's recommendations.

Western blotting

Snap-frozen samples from vehicle or MEKi treated control and mutant cerebella were homogenized in Pierce RIPA Buffer (Thermo Scientific) (10 μl buffer/1 mg tissue) for 20 min on ice, then subjected to centrifugation at 14,000 rpm for 10 min at 4°C. The supernatant was mixed 1:1 with Laemmli Sample Buffer (BioRad, Hercules, CA) and boiled at 100°C for 10 min. Samples were then subjected to SDS-PAGE using the Criterion TGX Precast gels (BioRad) and transferred onto PVDF membranes (EMD Millipore). Membranes were blocked in 5% non-fat milk prepared in 1X TBST and incubated with primary antibodies at 4°C overnight. The following day, the membranes were washed with TBST and incubated in horseradish peroxidase (HRP)-conjugated secondary antibodies at room temperature for 1 h. The membranes were then exposed to Pierce ECL western blotting substrate (Thermo Scientific) for 3–5 min to detect signal by film development in dark room. The primary antibodies used in this study were:
p-Erk1/2$^{T202/Ty204}$ (9101S, 1:1,000, rabbit, Cell Signaling),
Erk1/2 (9102L, 1:1,000, rabbit, Cell Signaling),
pAkt^{S473} (4060L, 1: 1,000, rabbit, Cell Signaling),
Akt (9272S, 1: 1,000, rabbit, Cell Signaling),
p-S6 (5364S, 1: 2,000, rabbit, Cell Signaling),
S6 (2217S, 1: 2,000, rabbit, Cell Signaling),
β-Actin (A5316, 1: 20,000, mouse, Sigma-Aldrich).

Flow cytometry

Optic nerves/chiasm, and blood from MADM mice were collected at postnatal day 15, 21, and 30. Tissues were transferred to Cold Activated Protease buffer (500μg/ml *Bacillus Licheniformis*, 5mM $CaCL_2$, 12.5U/ml DNase I, 1X PBS) and incubated on ice for 15 min with intermittent trituration. Cell suspension was filtered through a 70μm cell strainer and washed twice with 1X PBS. All subsequent procedures were performed on ice protected from light. Samples were resuspended in Live/Dead Aqua [1:500 in 1X PBS], incubated for 30 min, and washed with 1X PBS. Samples were resuspended in FACS staining buffer (1X PBS, 0.1% FBS, 0.01% Sodium Azide)

and Fc-block (BioLedend, San Diego, CA) for 15 min. Samples were washed twice in FACS staining buffer and acquired using a CytoFLEX S analyzer with CytExpert software (Beckman Coulter, Indianapolis, IN). Blood samples were incubated in ACK lysis buffer, followed by Live/Dead Aqua and PE- or FITC-conjugated anti-CD3 staining for gates setup. At least 10,000 - 50,000 live events were analyzed for red (tdTomato), green (GFP) fluorescence using FlowJo software (BD Biosciences, San Jose, CA).

ACK Lysis buffer (A10492-01, 2mL/test, Gibco)
Compensation beads (01-2222-42, 1 drop/test, Invitrogen)
Arc Amine Reactive Compensation Bead Kit (A10628, 1 drop for each/test, Invitrogen)
Live/dead Aqua fluorescent reactive dye (L34966A, 1:500, Invitrogen)
Fc receptor blocking (101320, 3ul/test, rat, BioLegend)
PE-anti-mouse CD3 (100206, 3ul/test, rat, BioLegend)
FITC-anti-mouse CD3 (11-0031-85, 3ul/test, hamster, Invitrogen)
PE-isotype control (12-4321-42, 3ul/test, rat, eBioscience)
FITC-isotype control (400906, 3ul/test, hamster, BioLegend)

QUANTIFICATION AND STATISTICAL ANALYSIS

Kaplan-Meir survival curves used to compare the survival of mice with different genetic manipulations of *Mek1/2*, with or without *Nf1* deletion were generated using GraphPad Prism. The Mantel-Cox (log-rank) and the Gehan-Breslow-Wilcoxon tests were used to statistically compare the overall survival.

When quantifying the optic nerve diameter, we used H&E-stained sections and imaged the thickest portion of the nerve starting from the chiasm for 100 uM at 20X magnification (adult nerves) or 40X magnification (embryonic or early postnatal). The area was measured using ImageJ (1.52c) image processing software, and cell number and density were quantified using the cell counter plugin in (https://imagej.nih.gov/ij/download.html).

For immunostaining quantification, multiple images from different mice were captured. For the quantification of embryonic (E17.5) MADM slides, three slides of the hypothalamic regions (covered 0.32 mm from the rostral to caudal positions) were analyzed. When possible, single-blind imaging and analysis was conducted. At least three animals from each group were used for quantification.

Statistical analysis was carried out using two-tailed parametric Student's t test in Graphpad Prism based on the Gaussian distribution observed in the data quantification. Data were presented as mean ± Standard Error Mean (SEM). $p < 0.05$ was considered to be statistically significant.

Venn diagrams were generated using EulerAPE (Micallef and Rodgers, 2014).